IMPLICATIONS OF RECENT BVI CALCULATIONS ON PREDICTION METHODS FOR NOISE FROM TURBULENCE INGESTION

Prepared by:

Sheryl M Grace
(With assistance from **Trevor H. Wood***)

ASEE Summer Faculty Researcher, NSWC, Carderock Division
Department of Aerospace and Mechanical Engineering
Boston University
110 Cummington St.
Boston MA, 02215
(*Research Assistant, Dept. AME, BU)

August, 2000

Prepared for:

Robert Minniti, Code 70

NSWC, Carderock Division
9500 MacArthur Blvd.
West Bethesda, MD 20817-5700

Contents

List of Figures

1 Summary

A general method for analyzing the response spectrum of a lifting surface has been developed. The method relies on the boundary element method (i.e. panel method) to compute the response of a blade section to an imposed disturbance. The response is computed in the time domain and then Fourier transformed in order to obtain the frequency spectrum.

The main goal of this research has been to validate and extend the previously reported results of Martinez.[1] (This reference will be indicated as [1] throughout this report). Martinez studied analytically the response of Joukowski blade shapes to an incident vortex. The imposed incident vortex (as opposed to an incident gust) allows easy analysis of the response to a broad band disturbance. He showed, that using this method one can predict the decrease in blade response as the blade thickness increases. (This result is not predicted using the single frequency gust response methods.) A decrease in the response with increased camber was also noted. Finally, he noted that the response spectra for various geometries and flow conditions included nulls at certain frequencies.

Because of the analytical nature of the Martinez blade-vortex-interaction (BVI) solution, only Joukowski blade geometries were analyzed. When a general method such as the boundary element method (BEM) is applied to the problem, many different blade geometries can be studied. Here a two-dimensional BEM calculation has been adopted to predict the blade section response to an incident vortex. This report discusses the following salient results from simulations using the BEM method.

- The method is validated against the analytical response of a flat plate, at zero incidence angle, to a passing vortex.
- The predicted unsteady surface pressure for a thick, symmetric blade section is qualitatively compared to experimental results. (A quantitative comparison will be completed when information concerning specifics of the experiment are obtained.)
- The method is validated for the Sears problem.

  From these three validations, it was determined that the method is working properly.
- The implications of computing the BVI response using the rapid distortion theory (employed by Martinez) as opposed to allowing the incident vortex to evolve freely are discussed.

  It is shown that the response spectrum is well behaved when the disturbance strength is chosen such that there is compliance with the disturbance constraints implied in rapid distortion theory.
- Several cases reported in [1] were rerun.

  The response reduction with increasing thickness and camber is captured; however, the nulls in the response spectrum cannot be validated nor invalidated using the current method.

- The response of a geometry of interest to the Navy has been computed in order to exemplify the capabilities of the method.
- Three blade section geometries currently under experimental consideration at Carderock were analyzed.

  The response of these three blades to an incident vortex are effectively identical.

This research serves as a launching point for studying, more exactly, blade response to turbulence ingestion. The single incident vortex can be replaced by a cloud of vortices. If this cloud is formed correctly, the induced normal wash on a blade section can simulate a turbulent inflow. In addition, finite span effects can be studied by fully developing the three dimensional computational counterpart to that discussed in this report.

2 Introduction

A general picture of the problem is given below in Figure 2.1. A single vortex follows a path from upstream, past the blade section, and proceeds downstream. A wake is shed continuously and the strength of the dipole along the wake (not apparent in the figure) is proportional to the change in lift at every time step. The figure depicts the total path followed by the vortex and the wake path. The insert in the top figure shows the lift response as a function of time and is aligned such that the response as the vortex passes the blade section is easily assessed. The lower figure shows the Fourier transform of the time domain response.

A boundary element method is used for the calculations in this research. This is a popular method for solving the BVI problem. Every edition of the Journal of the American Helicopter Society has at least one article regarding a BVI calculation. Most of the literature computes blade response to vortex interaction in the time domain. Unique to the work presented in this report is the extensive frequency domain analysis associated with the predicted response. In addition, this report contains an in depth analysis of the difference between the rapid distortion method of vortex evolution and free vortex evolution. Usually, those studying BVI noise with boundary element techniques apply free vortex evolution and those studying it using a linearized Euler approach automatically apply rapid distortion theory. The analysis presented here shows where these two method overlap.

The results of this research confirm that the BVI response spectrum at higher frequency decays as an exponential function of the form e^{-kl} where k is the normalized frequency and l is an appropriate length. The suitable length l for a vortex passing a flat plate is the distance between the vortex and the plate. This spectral relation has previously been shown analytically by Howe[2] and Martinez.[1] For thick and/or cambered airfoils however, l is not the distance to the airfoil boundary, but instead the distance to the mean camber line.

The results also give some indication as to why the frequency domain gust response calculations do not capture the reduction in response at high frequency due to increased blade thickness. It is shown that the phase of the induced normal wash from a point vortex (especially the high frequency component) can vary greatly from the assumed $e^{-ik_1x_1}$ phase relation along the chord. Another important aspect however, is the difference in the magnitude of the induced downwash from suction to pressure side. Assume a thick symmetric airfoil is encountering a transverse gust. In a frequency domain simulation, the phase can and does vary from the flat plate canonical form ($e^{-ik_1x_1}$). However, the magnitude of the induced wash would be the same from pressure to suction sides. The method for introducing asymmtry from side to side is the introduction of a longitudinal gust component which is often left out of the frequency domain simulations.

Chapter 3 describes the computational method used in this research, with most of the mathematical details relegated to Appendix A. Chapter 4 discusses the validation of the method and some numerical implications on the question of the validity of the nulls. Chapter 5 shows the comparison between computations relying on rapid distortion theory and those allowing the imposed vortex to evolve freely. Chapter 6 compares results obtained using this method and the previously reported results of Martinez. Results for geometries of interest

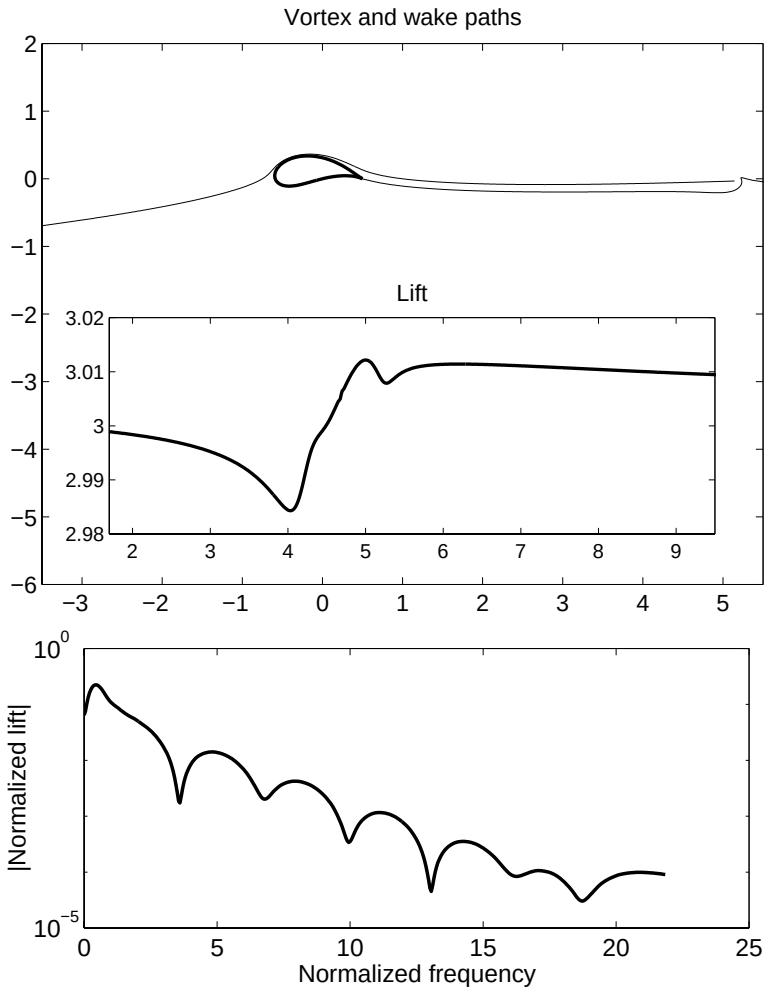

Figure 2.1: Problem example. Time domain response (top). Frequency domain response (bottom).

to the Navy are reported in Chapter 7. And finally, possible extensions of this work are discussed in Chapter 8.

3 The Method

The present research uses a two-dimensional adaptation of the boundary element method (BEM) as formulated for quasi-potential flows.[3,4] The flow is modelled as potential everywhere off of the solid blade section and outside the wake. Fully attached, high Reynold's number flows are assumed such that viscous effects are prevalent only in the wake generation at the trailing edges of the blade section. The flow velocity infinitely far from the blade section is taken to be uniform in the x_1 direction and to be incompressible.

Under the above assumptions, with the added generalization of compressible flow, the perturbation velocity potential is known to satisfy the convective wave equation[5]

$$M^2 \frac{D_\infty^2 \phi}{Dt^2} - \nabla^2 \phi = 0, \tag{3.1}$$

where space and time have been scaled by the reference chord length c and the convective time scale c/U_∞, respectively. The solution to Eq. (3.1) satisfies the boundary integral equation

$$-\frac{1}{2\pi} \int_{\tilde{S}} \left[\ln r \frac{\partial \tilde{\phi}(\tilde{\mathbf{y}}, \tau)}{\partial \tilde{n}} + \frac{\tilde{r} \cdot \tilde{n}}{\tilde{r}} \left(\frac{\tilde{\phi}}{\tilde{r}} + \frac{\dot{\tilde{\phi}}}{\tilde{a}} \right) \right]^{\tau^\star} d\tilde{\mathbf{y}} = \begin{cases} \tilde{\phi}(\tilde{\mathbf{x}}, \tilde{t}) & , \text{ for } \mathbf{x} \text{ in field} \\ \frac{1}{2}\tilde{\phi}(\tilde{\mathbf{x}}, \tilde{t}) & , \text{ for } \mathbf{x} \text{ on wing} \\ 0 & , \text{ for } \mathbf{x} \text{ ins ide wing} \end{cases} \tag{3.2}$$

where $\tau^\star = \tilde{t} - \tilde{r}/\tilde{a}$, $\tilde{a} = \beta/M$, $\beta = \sqrt{1 - M^2}$, $\tilde{r} = |\tilde{\mathbf{x}} - \tilde{\mathbf{y}}|$, and tildes denote evaluation in the Prandtl-Glauert space—

$$\left(\tilde{\mathbf{x}}, \tilde{t}\right) = \left(\frac{x_1}{\beta}, x_2, t - \frac{M^2 x_1}{\beta^2} \right). \tag{3.3}$$

Equation (3.2) is solved numerically by applying a zeroth-order boundary element method and linear time interpolation to give a set of algebraic equations[6]

$$H \phi_i^n = \sum_j G_{D_{ij}}^{(B)} \phi_j^{n-\tau_{ij}} - G_{S_{ij}}^{(B)} v_{n_j}^{n-\tau_{ij}} + G_{R_{ij}}^{(B)} \dot{\phi}_j^{n-\tau_{ij}} + G_{D_{ij}}^{(W)} \Delta \phi_j^{n-\tau_{ij}}, \tag{3.4}$$

where,

$$\tau_{ij} = \frac{M}{\beta} \left(r_{\beta_{ij}} + M r_{1_{ij}} \right), \tag{3.5}$$

$$r_{\beta_{ij}} = \sqrt{(x_{i_1} - y_{j_1})^2/\beta^2 + (x_{i_2} - y_{j_2})^2}. \tag{3.6}$$

The indices i, j, and n refer to the collocation point, panel index, and time iteration, respectively. The blade and wake surfaces are denoted by (B) and (W), and G_S, G_D, and G_R refer to the source, doublet and ratelet influence matrices. By applying equations (3.4) to collocation points located at the center of each panel on the body, a time-domain solution for the surface distributions of ϕ is readily obtained. The flow velocity and pressure may then be determined through differentiation and Bernoulli's equation.

The solid surfaces of the blade section are impermeable. Thus, the normal perturbation velocity is required to satisfy

$$\mathbf{U}_\infty \cdot \mathbf{n} + \frac{\partial \phi}{\partial n} = 0. \tag{3.7}$$

The wakes are modelled as infinitely thin shear layers and, therefore, cannot support a pressure jump. By applying Bernoulli's equation to a point $\mathbf{x}_+$ just above and $\mathbf{x}_-$ just below the wake, one obtains

$$\frac{\partial \Delta\phi}{\partial t} + \frac{1}{2}(v_+^2 - v_-^2) = \frac{\partial \Delta\phi}{\partial t} + \frac{\mathbf{v}_+ + \mathbf{v}_-}{2}(\mathbf{v}_+ - \mathbf{v}_-) = \tag{3.8}$$

$$\frac{D_w}{Dt}(\Delta\phi) = 0, \tag{3.9}$$

where

$$\frac{D_w}{Dt} = \frac{\partial}{\partial t} + \mathbf{v}_w \cdot \nabla = \frac{\partial}{\partial t} + \frac{\mathbf{v}_+ + \mathbf{v}_-}{2} \cdot \nabla. \tag{3.10}$$

Equation (3.9) is the condition which relates the wake strength $\Delta\phi$ to the potential jump at the trailing edge when the wake element was located at that trailing edge. Additionally, the wake evolution is determined such that the fluid elements in the wake are convected with the average velocity across the sheet. This defines a *free-wake* evolution which is described in greater detail in Wood and Grace[7] and Ramsey.[8] The free-wake evolution is easily implemented assuming incompressible flow ($M = 0$). Compressible free-wake evolution is more difficult and has not been implemented. For a more detailed derivation of the general, three-dimensional, compressible flow governing equations and the formation of the numerical approach, see Appendix A.

All of the computations reported in the following chapters were performed for two-dimensional geometries assuming incompressible flow and allowing for free-wake evolution (unless otherwise noted).

4 Transform method and Validation

To determine whether the current BEM calculation was working correctly for the BVI problem, the flat plate simulation was run and compared to the analytical solution. The analytical lift response of a flat plate to a passing vortex is given by

$$\rho,\ \frac{c}{2}e^{-kh}\frac{1}{\pi k}\frac{1}{\left(H_1^{(1)}(k)-jH_0^{(1)}(k)\right)} \tag{4.1}$$

where $k = \frac{\omega c}{2U}$ is the normalized frequency, U is the freestream speed far upstream, h is the distance from the plate to the path of the vortex, , is the strength of the vortex, and $j = \sqrt{-1}$. H_ν is the Hankel function of order ν [1].

The computations are performed for a NACA 0001 blade section. (This simulates a flat plate well.) Once the simulation is complete, the lift response (which is calculated as a function of time) is Fourier transformed into the frequency domain. The analytical solution, Eq. (4.1), requires that the time variable reference 0 when the vortex passes the midchord of the blade section. Thus, before transforming the computed result, the time variable must be shifted to account for the zero reference. In addition, the analytical result assumes a length scale of half chord which affects the time, frequency, and lift normalizations. Therefore, a rescaling of the computed time domain results may be necessary, if the same length scale is not used in the computation.

After scaling and referencing time zero correctly, the computed results are transformed to the frequency domain. A Hanning window is used in conjunction with the Fourier transform. It is used because the computation is run for a finite time. The finite time implies that the blade section is producing lift due to the presence of the vortex from the instant the simulations starts and still when the simulation is stopped. One can see this in Figure 2.1. The results are not adversely affected by the windowing when the vortex strength is smaller and the vortex starts more than two or three chordlengths upstream and is allowed to travel the same distance downstream. (An example is the simulation shown in Fig. 2.1 where the vortex amplitude is 0.02, and it starts 4 chordlengths upstream.)

Figure 4.1 compares the computed and analytical response for a vortex passing above the flat plate at a distance of 4% of the half chord and for a vortex passing at a distance of 60% of the half chord. The real and imaginary part of the transform as well as the magnitude is compared against the analytical solution in Figure 4.2. Finally, the magnitude of the response in the frequency domain is shown.

The agreement between the computed and analytic results for the vortex passing closest to the flat plate is very good. However, the low frequency singular behavior is not captured using the BEM method (i.e. below a normalized frequency of 0.5). Some phase error exists for the case when the vortex path is far from the plate. This error is attributed to the small amplitude of the response in time. When the response has too low of an amplitude, the Fourier integration suffers. Throughout this report, either the vortex path's closest passing distance is within at most 20% of a half chord from the airfoil, or the amplitude of the vortex is taken to be a larger number. These parameters ensure accurate predictions from the numerical simulation.

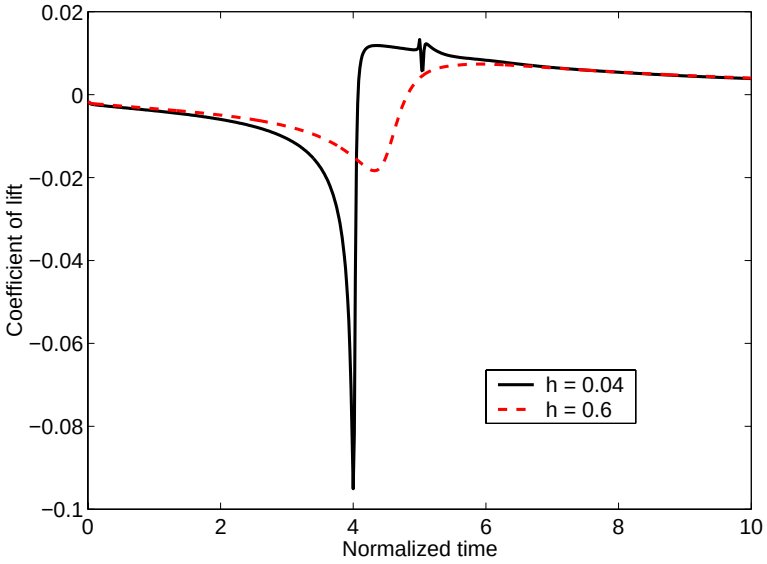

Figure 4.1: Coefficient of lift vs. time for vortex passing flat plate at two different distances.

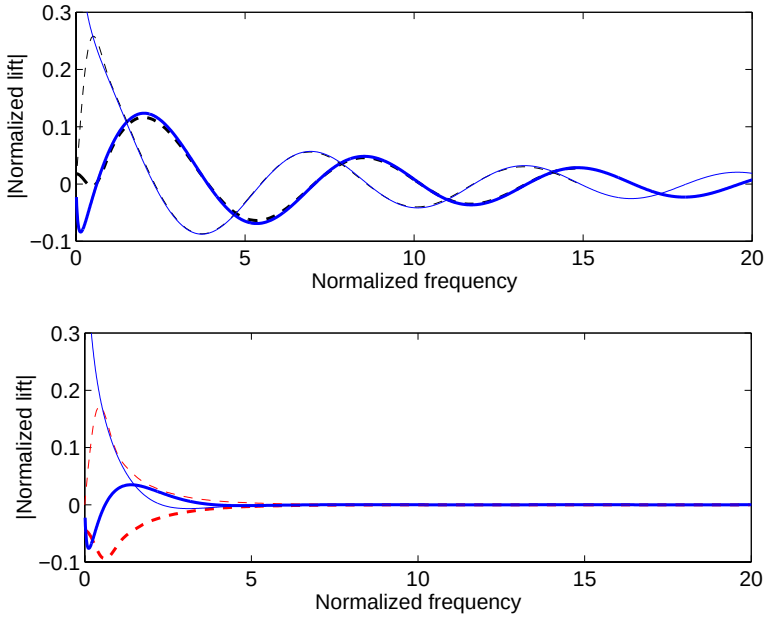

Figure 4.2: Real (thick line) and imaginary (thin line) part of Fourier transform for the analytical result (solid line) and the computed result (dashed line). Top is the case when the vortex is passing close to the plate, and bottom is when it passes farther away from the plate.

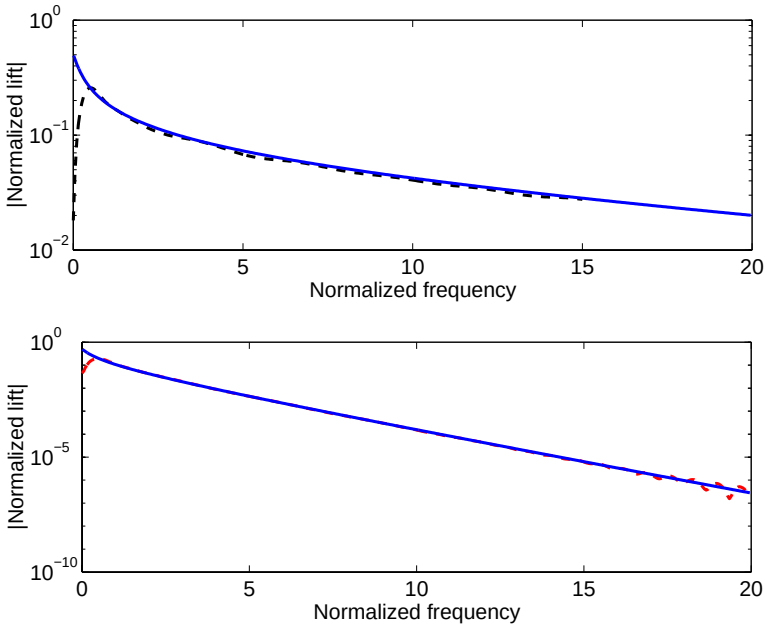

Figure 4.3: The analytical magnitude of the response (solid line) and the computed response (dashed line). Top is the case when the vortex is passing close to the plate, and bottom is when it passes farther away from the plate.

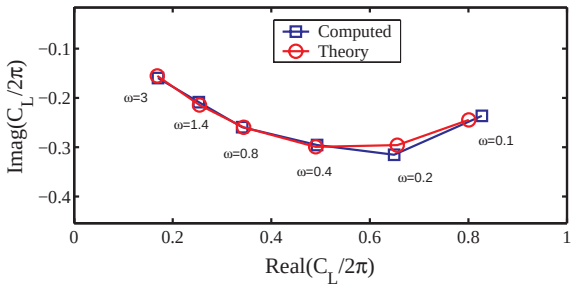

Figure 4.4: Computed and analytical coefficient of lift for Sears problem at various normalized frequencies.

The computation was also validated using the classical Sears problem. A very thin, symmetric airfoils was used, and the Sears normal velocity condition was applied along the airfoil surface. The solution was transformed to the frequency domain and the amplitude of the response at the imposed harmonic was compared to the analytical solution. Figure 4.4 shows the real and imaginary parts of the computed response compare very well with the analytical solution.

Experimental BVI results performed for an informal meeting of researchers from the field of helicopter rotor research offer a second qualitative validation. The parameters of the experiment were not available at the time this report was prepared. However, some results were presented in a paper by Rule, Epstein, and Bliss.[9] From their paper, it was clear that the blade section was a NACA 0012. However, the strength of the vortex and its distance from the airfoil are not known. Figure 4.5 shows the coefficient of pressure at points on the suction and pressure surfaces for the 2% chord location, the 11% chord location and the 40% chord location. The most noticeable feature in the NASA experimental curves, is the

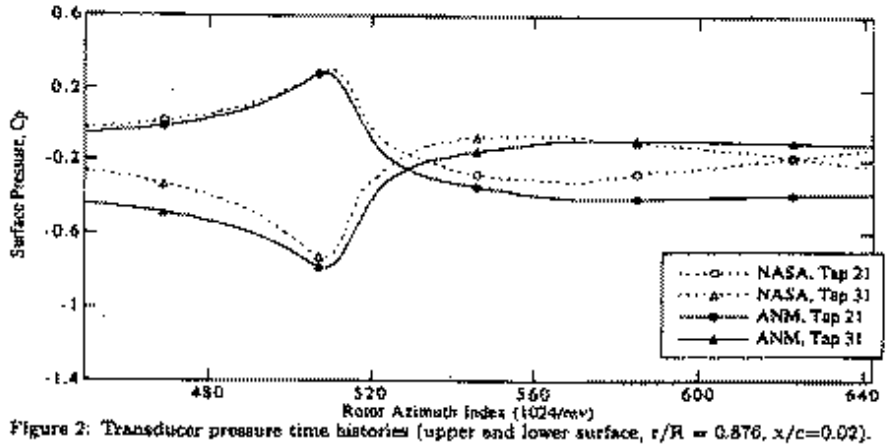

Figure 2: Transducer pressure time histories (upper and lower surface, r/R = 0.876, x/c=0.02).

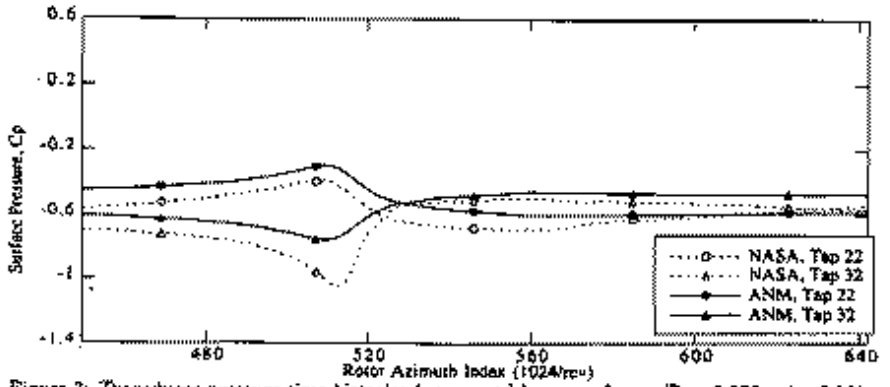

Figure 3: Transducer pressure time histories (upper and lower surface, r/R = 0.876, x/c=0.11).

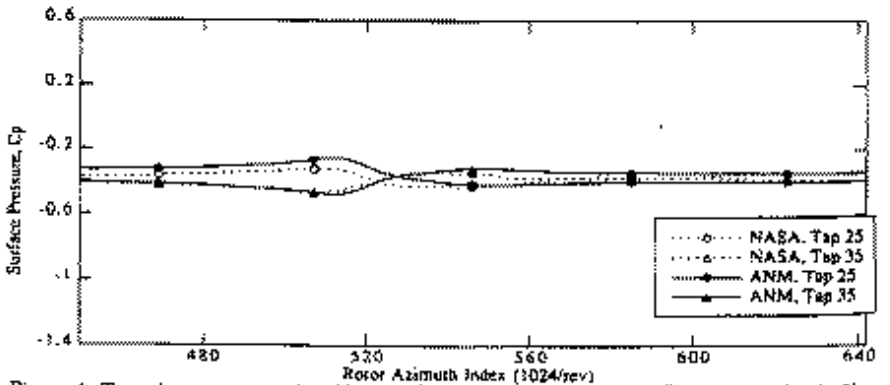

Figure 4: Transducer pressure time histories (upper and lower surface, r/R = 0.876, x/c=0.40).

Figure 4.5: Reproduced from ref. 9. Coefficient of pressure in time as vortex passes the blade section.

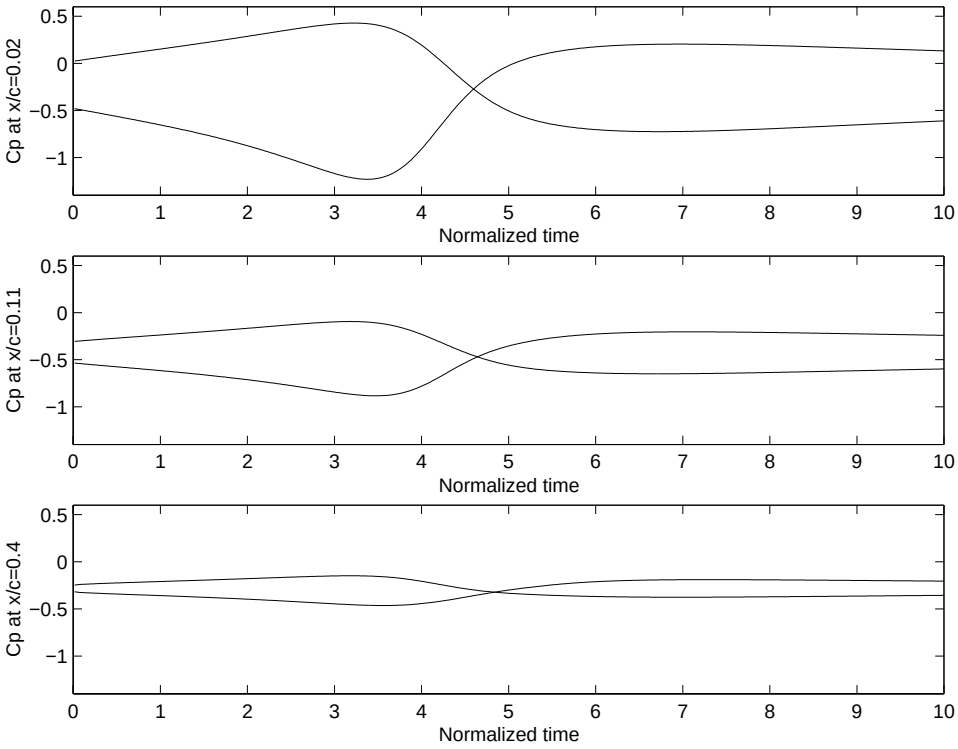

Figure 4.6: Coefficient of pressure from NACA 0012 simulation with vortex of strength 1.0 passing at a distance of 1 chord.

asymmetry from top to bottom. This asymmetry appears when a generic simulation is run using the current method. Because the experimental parameters are not known, a vortex at 1 chord above the airfoil with strength 1.0 was simulated. The surface pressure plots at the 3 chord locations of interest are shown in Figure 4.6.

4.1 Discretization and occurrence of nulls

Martinez[1] showed the occurrence of nulls in the unsteady lift spectrum for a vortex passing thick, heavily cambered airfoils at a high angle of attack. Figure 4.7 is a reproduction of a result from [1]. The nulls have been attributed to phase cancellations. However, another figure, 4.8, from the Martinez report, indicated that the occurrence of nulls is not a uniform process. It was hoped that this research would validate these nulls and help to understand the generating mechanism.

In the present computational method, the occurrence of nulls is shown to be partially linked to the discretization method. This is demonstrated by using a NACA 0012 airfoil. The airfoil chord runs from -0.5 to 0.5 on the x-axis. A vortex of nondimensional strength 0.02 is imposed on the flow field at an upstream location of (-4.5, 0.03). The upstream flow is normalized to unity. The vortex is allowed to convect freely and its closest approach to the airfoil is a distance of 0.0192 (based on a half chord of 0.5). This compares to a closest approach of 0.0384 in the Martinez report where the airfoils run from -1.0 to 1.0.

The response in time for three different airfoil discretization methods is shown in Figure 4.9. Linear spacing refers to equal spaced dx discretization along the chord of the airfoil.

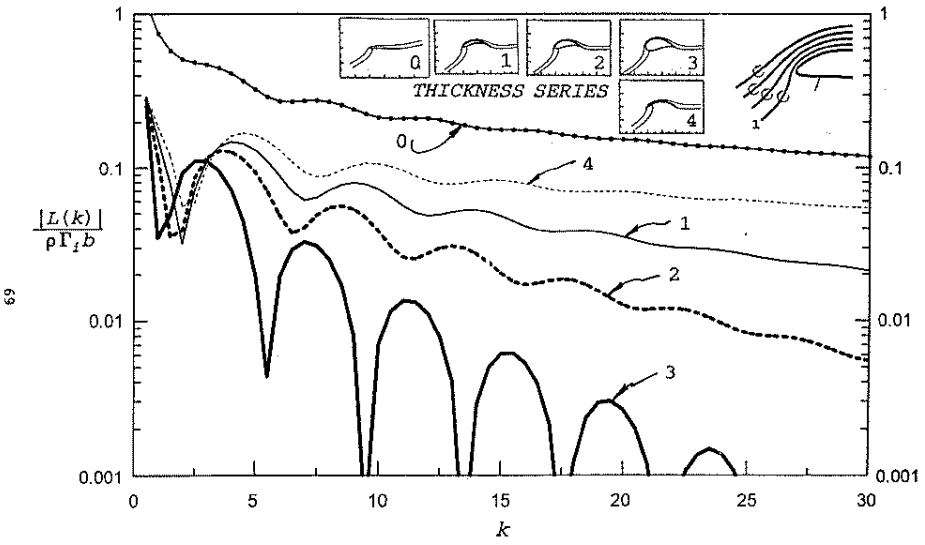

Figure 4.7: Figure 16b from [1]. Occurrence of nulls in the lift response for the thickest airfoil considered. Closest streamline. Angle of attack 20°.

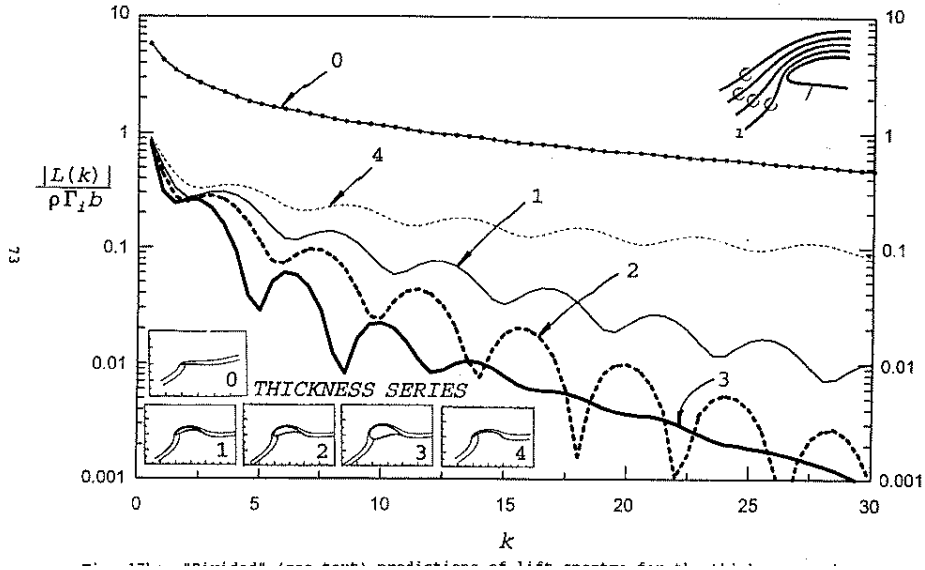

Figure 4.8: Figure 17b from [1]. Occurrence of nulls in the lift response. Closest streamline. Angle of attack 5°

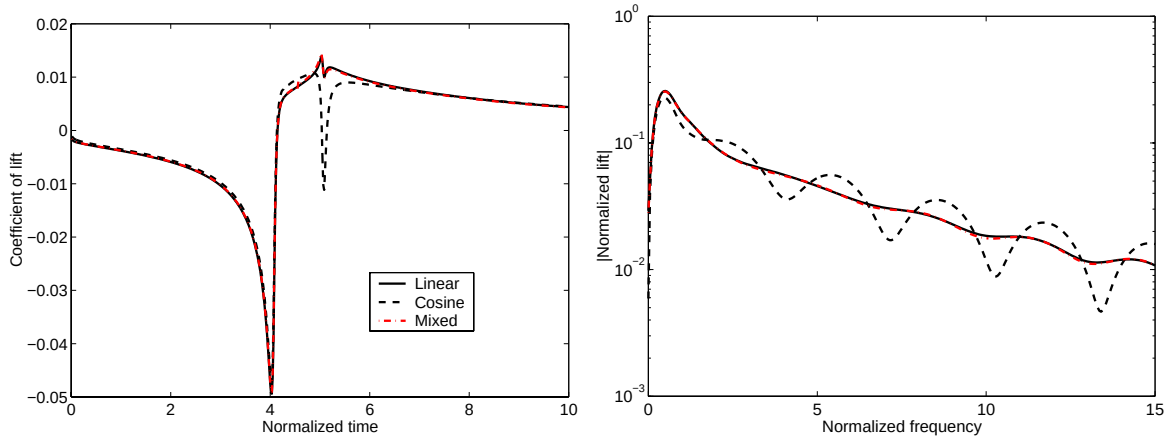

Figure 4.9: Coefficient of lift (left) and lift spectrum (right) computed using different airfoil discretizations.

Cosine spacing refers to equal spaced $d\theta$ discretization along the chord of the airfoil where $-\frac{c}{2}cos\theta = x$. The mixed discretization uses a cosine spacing from the midchord forward and a linear spacing from the midchord aft. Transforming these different response curves, one obtains the lift spectrum also shown in Figure 4.9. It is clear from these spectrum, that the cosine discretization which predicts a larger forced response as the vortex passes the trailing edge of the airfoil also predicts a much more scalloped frequency spectrum.

The main different between the linear and cosine spacings is their compatibility with the wake spacing. At each time step a wake panel is shed. These panels have a length, determined by the convection speed, which is close to Udt. For the linear spacing, the body panels forward of the trailing edge are similar in length to the wake panels aft of the trailing edge. Body panels near the trailing edge determined from a cosine spacing however have lengths much shorter than the wake panels. It is believed that it is this incompatibility in the panel spacings near the trailing edge which is responsible for the large amplitude response predicted when using a cosine spacing.

Studying this effect further shows that the cosine spacing is not as robust to changes in the number of body panels nor changes in the wake panel lengths. First, the coefficient of lift as a function of time is shown for several different levels of body discretizations. Figure 4.10 shows various cosine spacings and Figure 4.11 shows results from various linear spacings. (These are all produced with a fix time step (i.e. fixed dt and thus fixed wake panel length).

A similar comparison is shown with the number of body panels fixed, but the time step changed slightly. Figure 4.12 show the impact of a change in time steps. Recall that the time step affects the value of dt which is associated with the wake panel lengths through the convection distance Udt.

The results are more robust to discretization changes when the linear spacing is used at the trailing edge of the airfoil. When this spacing is used, there are no nulls in the lift spectrum for the NACA 0012 at zero angle of attack. Because linear discretization makes it hard to capture the leading edge pressure rise, the mixed panel spacing with cosine spacing near the leading edge and linear near the trailing edge is used. Figure 4.9 shows that this discretization gives the same result as the linear discretization for the NACA 0012 case.

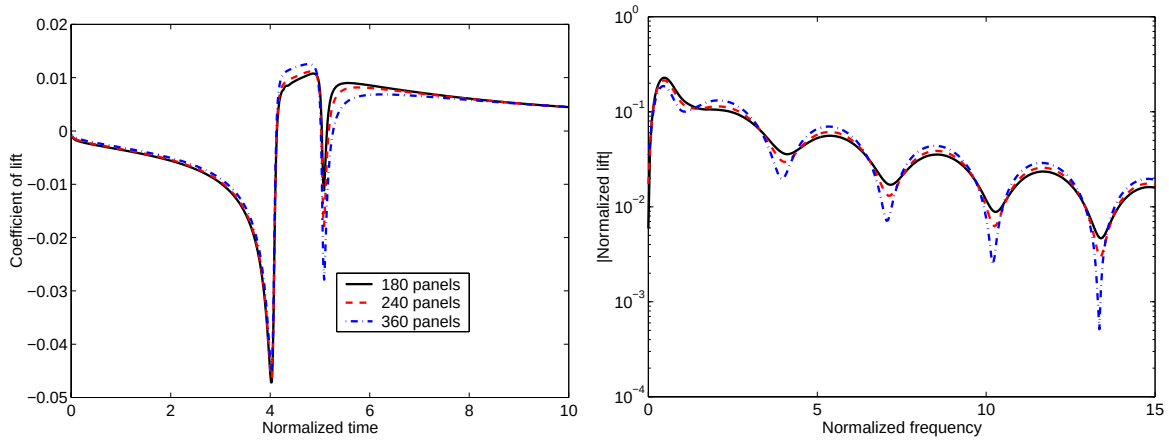

Figure 4.10: Effect of changing number of panels on coefficient of lift (left) and lift spectrum (right) when using cosine spacing. NACA 0012 airfoil.

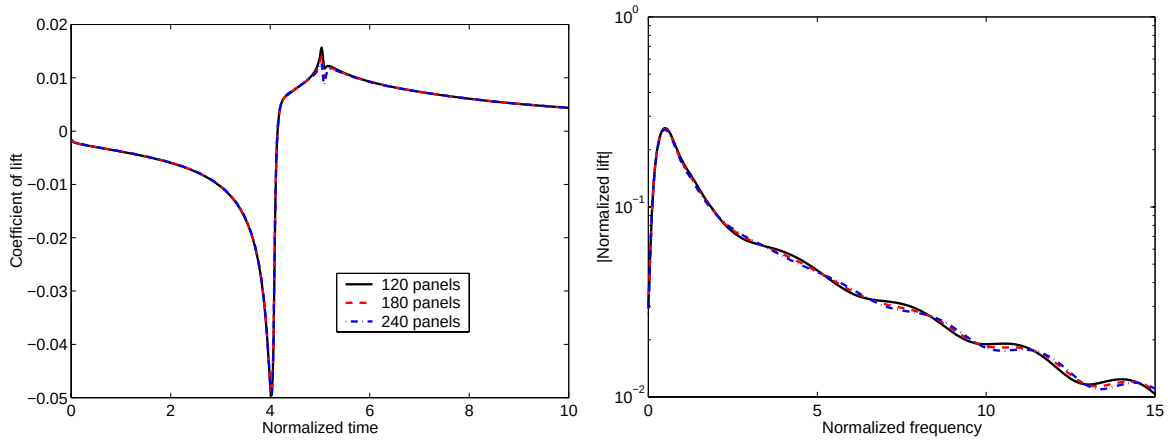

Figure 4.11: Effect of changing number of panels on coefficient of lift (left) and lift spectrum (right) when using linear spacing. NACA 0012 airfoil.

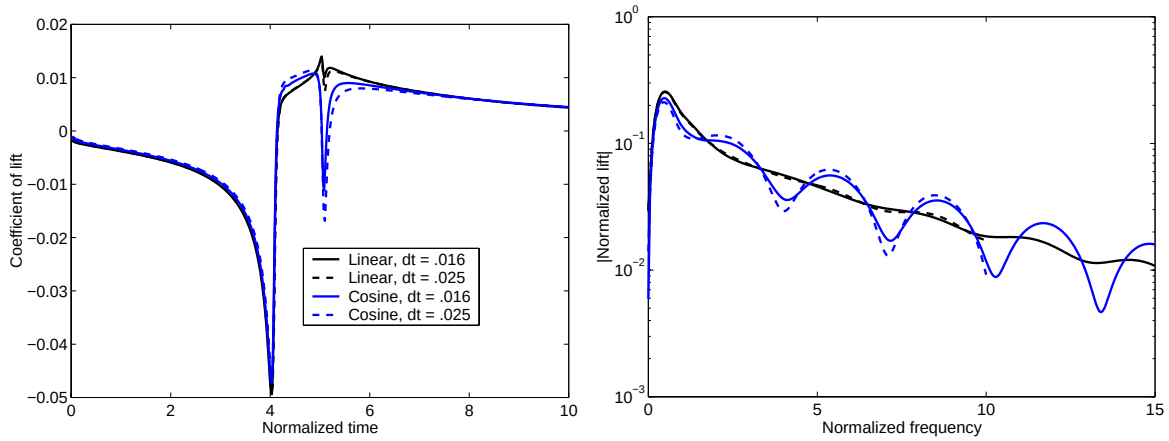

Figure 4.12: Effect of changing wake panel length on coefficient of lift (left) and lift spectrum (right) when using cosine and linear spacing. NACA 0012 airfoil.

However, it gives better results for thinner cambered airfoils where the pressure rise at the leading edge is larger.

For the computations in this report, the lift is obtained by using the mixed discretization (unless otherwise noted).

5 Effect of rapid distortion theory assumption

5.1 Magnitude of the disturbance

The rapid distortion theory (RDT) relies on the assumption that unsteady disturbances are a second order effect; that is, the mean flow can be separated from the fluctuating flow quantities and these fluctuating quantities will be carried solely by the mean flow and will not be influenced by other second order effects in the problem.

Using the current methodology, it is easy to assess the implication of this assumption on the BVI problem. Martinez, in his analytical treatment of the BVI problem, used an RDT assumption. He imposed a vortex on a mean flow streamline and allowed the vortex to follow the streamline at a speed dictated by the speed of the flow along that streamline. We can recreate this situation using the current computational method. First, the streamline is determined by following a vortex of zero strength. Then a vortex with given amplitude is forced to follow the same path as that mapped out by the zero strength vortex.

A blade section geometry used by Martinez is studied here. In [1], Case 2 is a Joukowski airfoil of chordlength 2.0 with input parameters of $S_R = -0.1$ and $S_I = 0.2$. The current simulation was run for the same Joukowski shape, however the shape was adapted to have a chord length of 1.0. The flow is set at a 20° incidence angle. The closest passing streamline analyzed for this case in [1] passes with a minimum distance of 0.044 (based on half chord of 1.0). After the streamline that satisfies this closest passing distance has been located, several cases were run using imposed vortices of different strengths. The coefficient of lift for the differing strength vortex simulations is shown in Figure 5.1. Under the assumptions of RDT, the lift curves should collapse to one curve when the magnitude of the vortex is normalized out. To make this comparison, a normalized lift is defined as

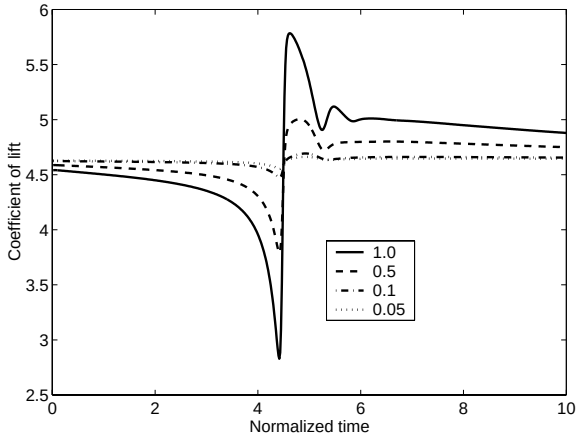

Figure 5.1: Coefficient of lift for various vortex strengths. All vortices follow same streamline path.

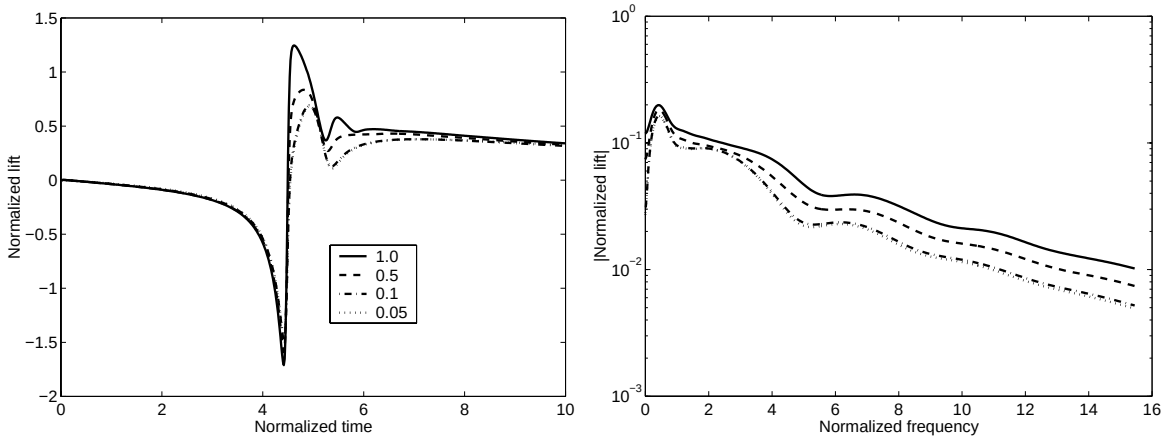

Figure 5.2: Normalized lift vs. time (left) and vs. frequency (right) for various vortex strengths. All vortices follow same streamline path.

$$\text{normalized lift} = \frac{C_l - C_{l_0}}{\frac{1}{2}\rho U^2 c,} \tag{5.1}$$

where , is the vortex strength and the subscript 0 denotes the steady (i.e. initial) coefficient of lift. The normalized lift is shown in Figure 5.2 For cases where the vortex strength is less than 10% of the freestream (i.e. vortex strength ≤ 0.1), the results collapse. The transform of the normalized lift is also shown in Figure 5.1.

5.2 Rapid distortion theory vs. free evolution

In the last section, the range of vortex strengths allowable for an RDT analysis to provide consistent predictions was discussed. Now, it is important to analyze the difference between simulations carried out using the RDT assumption and simulations that allow the imposed vortex to travel freely. Free evolution of the vortex will capture nonlinear interactions between the vortex and its effective images inside the solid boundary. It will also allow the vortex to be influenced by vorticity in the wake.

When the vortex evolves freely, one must iterate to determine the correct starting location for each different blade geometry and different imposed vortex strength in order to obtain a required minimum passing distance. This has been achieved for several vortex strengths. The coefficient of lift for several imposed vortex strengths are shown in Figure 5.3. Again, for fair comparison, the normalized lift is shown in Figure 5.4.

When results from the RDT and free evolution methods are compared, it becomes clear that for cases when the RDT theory is valid (i.e. vortices with strength no more than 10% of the freestream), both methods give similar response predictions. For example, see Figures 5.5 and 5.6.

Comparing the RDT results with result from [1], one can infer that in the previous research, vortex strengths of 1.0 were used in combination with the RDT assumption. Figure 5.7 shows the results for case 2 in [1]. The line labeled streamline 1 is the streamline that passes within 4.4% of a half chord of the blade section. This should be compared with the

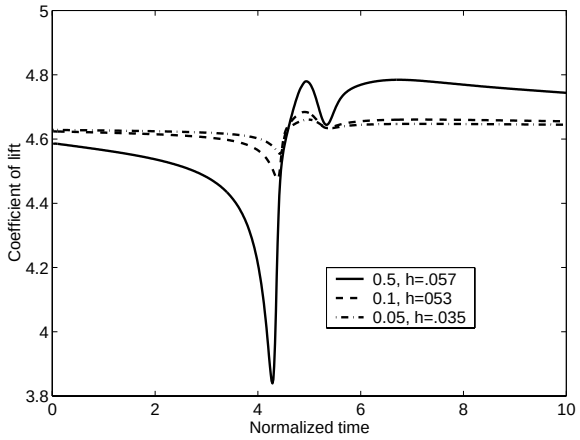

Figure 5.3: Coefficient of lift for various vortex strengths. Vortex evolving freely. Minimum passing distance retained.

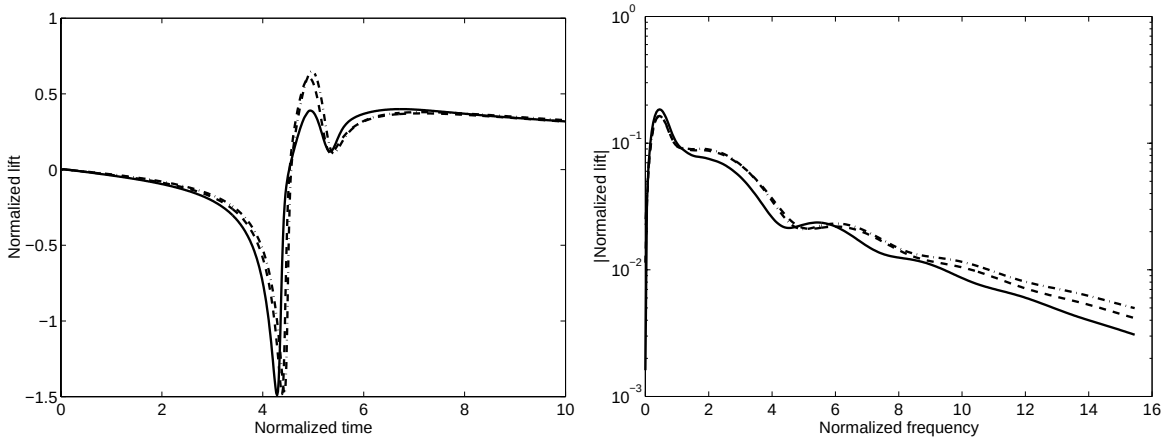

Figure 5.4: Normalized lift vs. time (left) and vs. frequency (right) for various vortex strengths. Vortex evolving freely. Minimum passing distance retained.

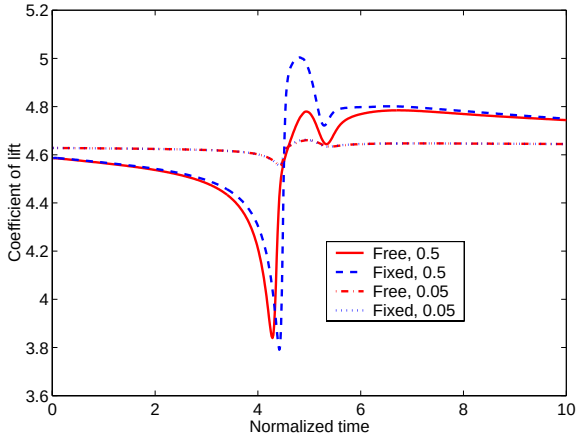

Figure 5.5: Coefficient of lift for various vortex strengths. Vortex path fixed and evolving freely.

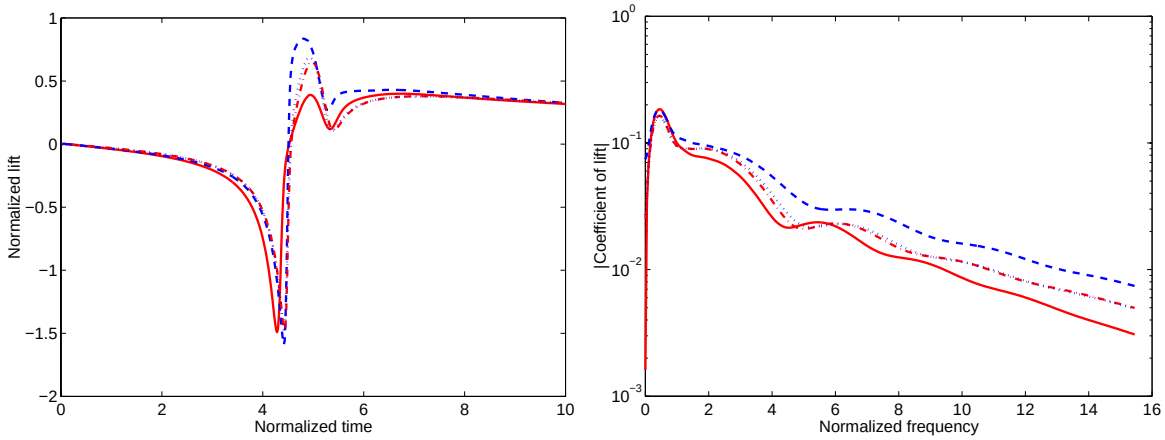

Figure 5.6: Normalized lift vs. time (left) and vs. frequency (right) for various vortex strengths. Vortex path fixed and evolving freely.

thick solid line in Figure 5.1. At a frequency of 15.0, both curves give a value of 0.01 for the magnitude of the response.

A vortex amplitude of 1.0 in the RDT method does not allow for the lift curves to collapse when normalized by the vortex strength. Also, it is easier to run the current simulation with a freely evolving vortex. Thus, all of the cases shown in the next sections have an imposed vortex strength of 0.02 and do not impose RDT. These simulations should compare well with RDT simulations because of the small vortex amplitude; however, results from the present calculations will not match identically the results reported in [1]. Instead, the predicted normalized lift will be much lower than that presented in [1]. The trends however, remain the same.

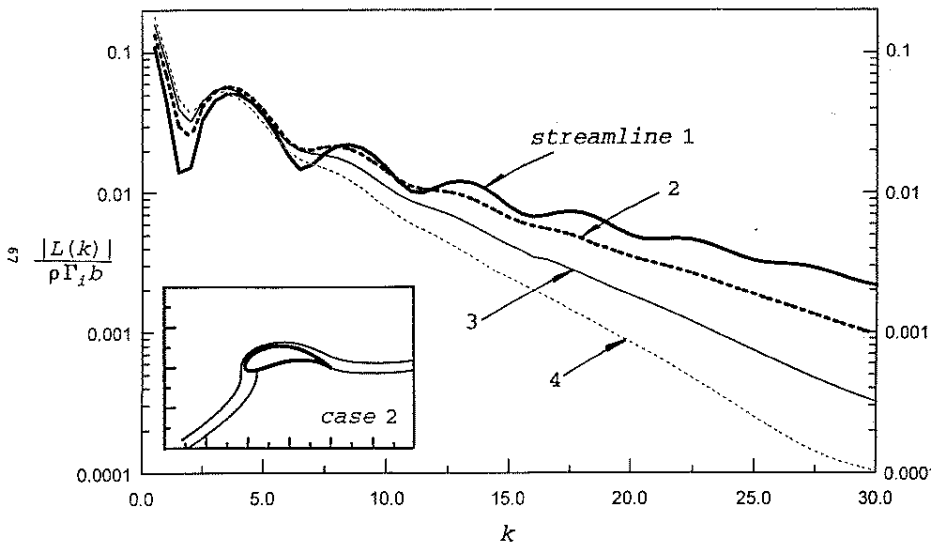

Figure 5.7: Figure 15b from [1]. Case 2, various streamlines.

6 Comparisons with previous predictions

Several simulations using the current method have been run in order to compare with the trends described in [1].

6.1 Vortex displacement effect

It was already shown in chapter 4, that when the vortex's minimum passing distance increases, the blade section response decreases. Another example of this phenomenon is included here. For a Joukowski airfoil described by case 2 in [1], a vortex of strength 0.02, passes by at varying minimum distances. The flow is at a 20° angle of attack. The response in time and the response spectrum is shown in figure 6.1. The trend of decreasing response with increased vortex passing distance is observed.

It is the vortex displacement from the mean camber line that governs the roll off of the response with frequency. The flat plate analytical response function contains the factor e^{kh} where h is the distance of the vortex path from the flat plate. From the results for other non flat plate cases, it is clear that the roll off is still with a factor e^{kl}. The l however for a general blade shape is the distance from the the vortex to the mean camber line at the vortex's minimum passing distance. This is demonstrated through example here. A vortex is imposed upstream of a NACA 0012 at 0° and 2° angles of attack. The vortex strength and starting location are kept fixed. The closest approach point for both cases is highlighted in Figure 6.2. At zero incidence angle, the distance from the mean camber line is roughly $l = 0.065$. Plotting the response spectrum with and without the $e^(-kl)$ factored out demonstrates that this is in fact the correct l to use. See Figure 6.3. The same can be shown for the 2° incidence case where the vortex distance from the mean camber line is roughly $l = 0.1$. A final case where a cambered NACA 1212 airfoil at 0° angle of attack is modelled with the same vortex parameters enforced. The vortex path and the response of

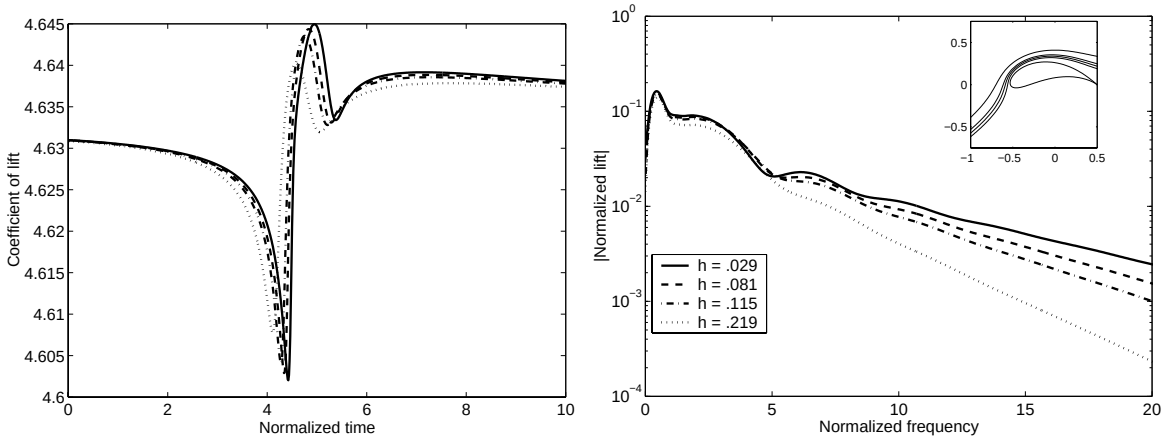

Figure 6.1: Response of Joukowski airfoil (Case 2 in [1]) to vortices passing at different distances.

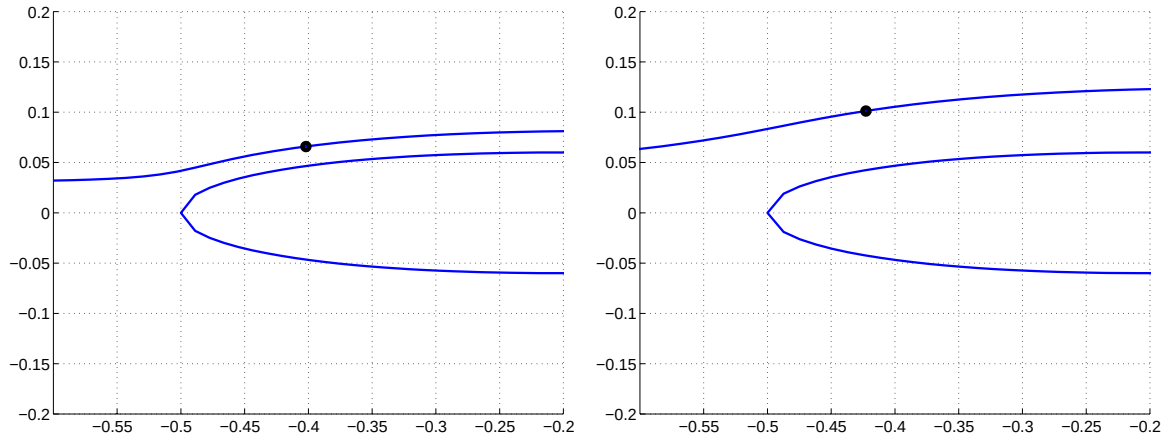

Figure 6.2: Vortex path and closest passing point for NACA 0012 at zero (left) and 2° (right) angle of attack. Vortex imposed as same upstream location for both cases.

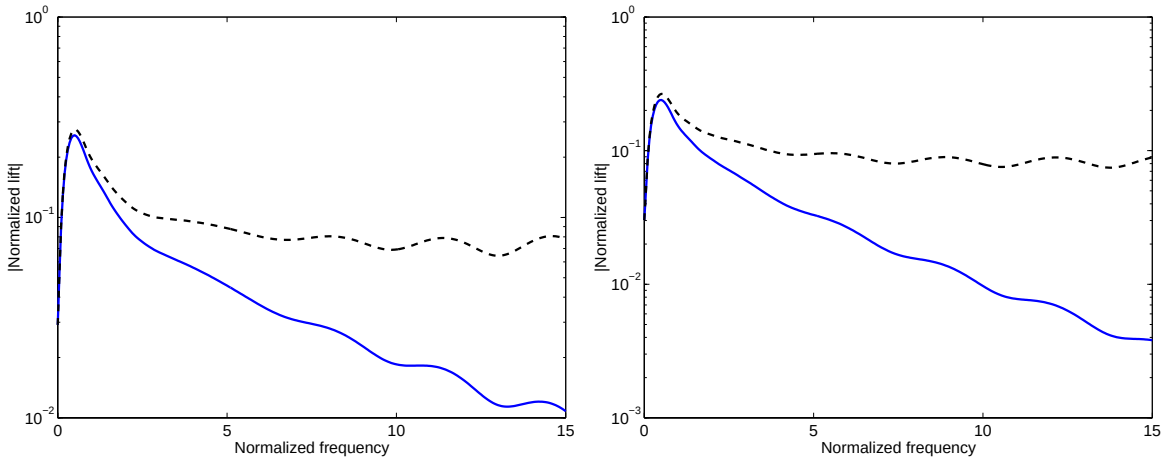

Figure 6.3: The response spectrum for the simulations in Fig. 6.2, with (dashed line) and without (solid line) the exponential factor taken out. Zero incidence angle (left), 2° angle of attack (right).

the blade are shown in Figure 6.4. The appropriate distance this time is roughly $l = 0.085$.

6.2 Thickness effect

The effect of thickness can also be captured with the current method. For a demonstration of this effect two airfoils, a NACA 0001 and a NACA 0012 are used. The vortex initial location is chosen such that the vortex passes with a closest distance of 4% of a half chord. The geometries and their associated vortex paths are shown in Figure 6.5. The coefficient of lift for the two simulations is shown as well as the transformed lift in Figure 6.6. The response of the NACA 0012 than that of the NACA 0001 is much less especially at higher frequency.

The thickness effect is also shown using a set of cases that were presented in [1]–Figure 16b. The blade sections appear in Figure 6.7. The flow is set to an incidence angle of

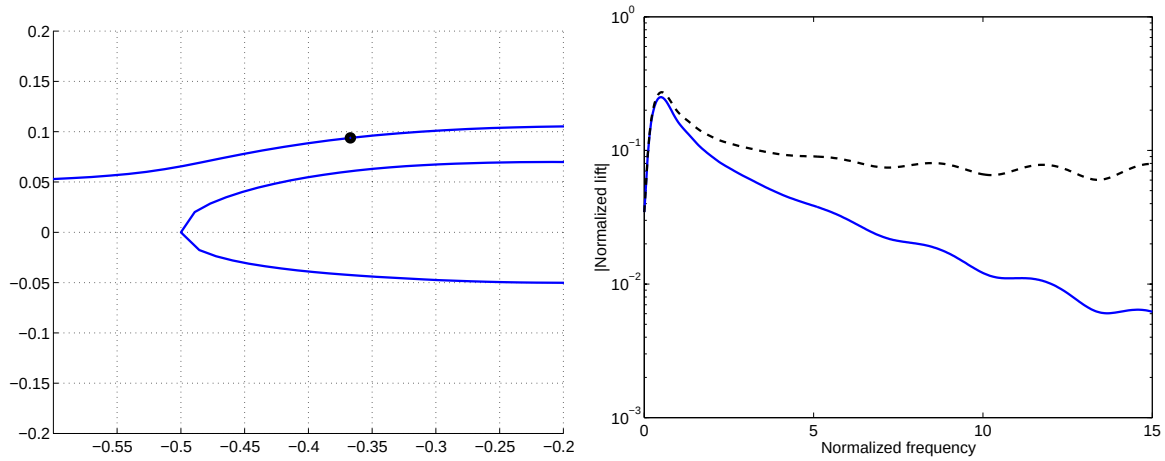

Figure 6.4: Vortex path (left) and response curve (right) for NACA 1212. Total response (dashed line), exponential factor suppressed (solid line).

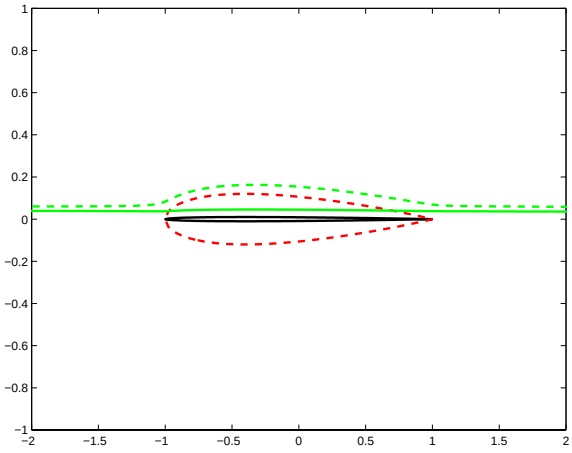

Figure 6.5: Response of the airfoils in time and their associated response spectrum.

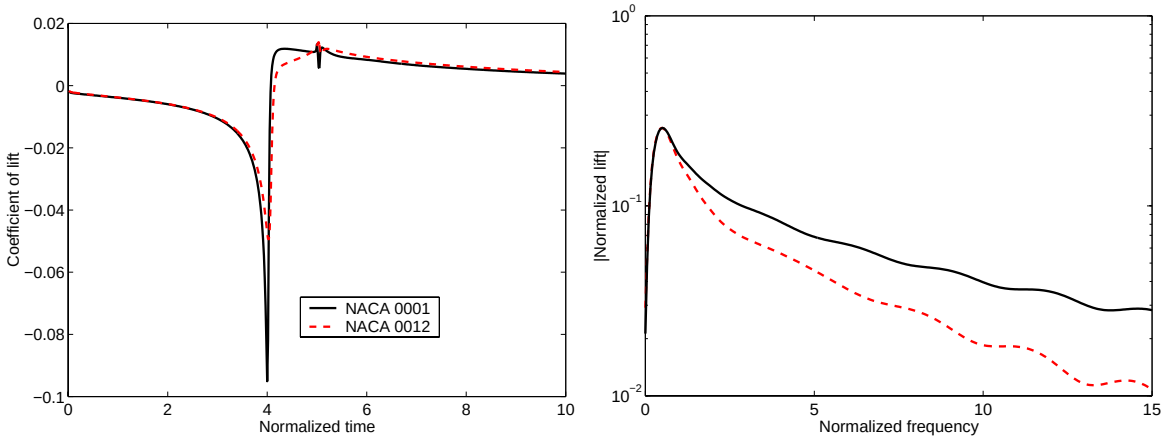

Figure 6.6: Response of the airfoils in time and their associated response spectrum.

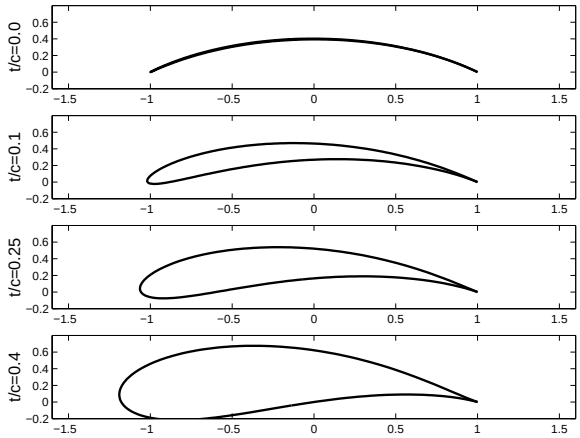

Figure 6.7: Airfoils used in thickness simulation.

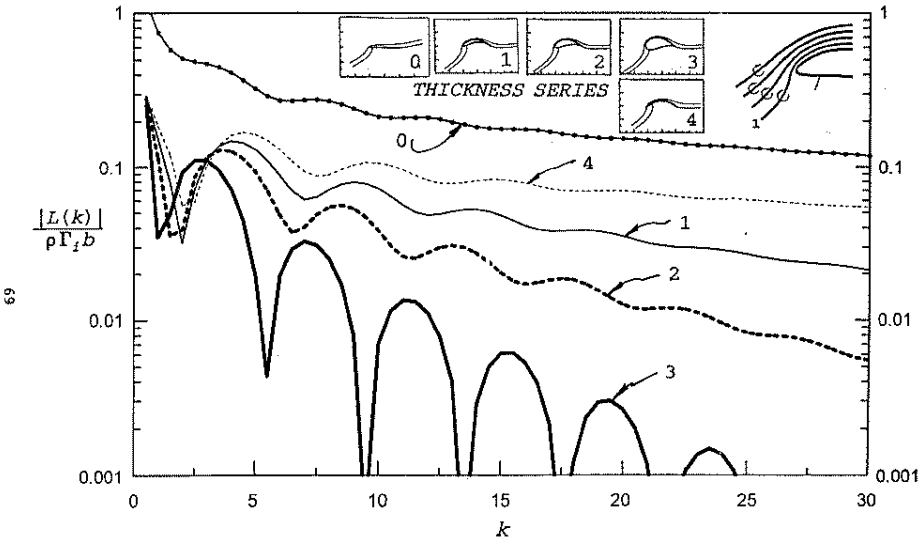

Figure 6.8: Figure 16b from [1]. Same as 4.7

20°. The closest passing for the different blade sections were matched to those used in [1]. They can be found in Appendix B which contains a reproduction of the cases chart from [1]. Figures 6.8 and 6.9 present the analytical prediction of Martinez and the time and frequency domain results from the current calculation. (Fig. 4.7 is repeated here for easy comparison.)

Note that the results in Figure 6.9 have also been normalized by the steady lift for each airfoil case. This gives a fair comparison of the unsteady response characteristics without biasing the comparison with the steady lift capabilities of the blade section.

The reduction in response with thickness is attributed to two causes. First, the magnitude of the induced normal wash due to the passing vortex is identical from pressure to suction side for the flat plate; but, for the thicker airfoil, the side closest to the passing vortex is influenced more strongly by the vortex. Second, the phase of the incident downwash along the plate is identically $e^{-ik_1 x_1}$; but, for the thicker airfoil, there is a departure from this

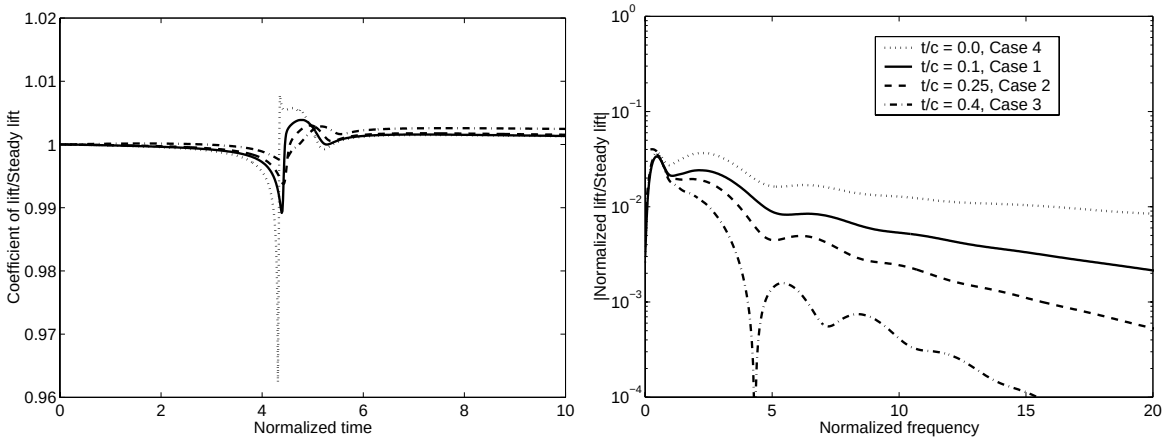

Figure 6.9: Response of the airfoils in time and their associated response spectrum.

Sears phase variation. Both of these effects are evident in Figures 6.10 and 6.11 where the magnitude and phase* $e^{ik_1x_1}$ at various frequencies is plotted. (The normalized frequency is noted to the left of each curve.)

The surface pressure resulting from the induced wash is also asymmetric from pressure to suction side for the thicker airfoil as seen in Figure 6.12. In addition, at higher frequency, the phase is quite different along the chord of the thicker airfoil, Fig. 6.13. The total lift is obtained by integrating the pressure jump along the body. Thus when the induced flow on the suction and pressure sides are simply π out of phase at each chordwise location and identically phased with $e^{-ik_1x_1}$, the maximum lift will be obtained. In other cases, the lift will be less. Finally, it is noted that the behavior of the phase of the pressure near the trailing edge is most likely incorrect. For the low values of pressure that occur at the trailing edge, numerical inaccuracies have swamped the actual values.

6.3 Effect of camber

A series of increasingly cambered airfoils was run and the results compared with the similar prediction in [1]. The airfoils are plotted in Figure 6.14. The time and frequency responses are shown in Figures 6.15-6.16. As was discussed in section 5.2, the predicted response values from the current method are smaller than those predicted in [1]. The pattern is undeniably the same though.

6.4 Effect of angle of attack

For this section, the case 3 airfoil from [1], was run at various angle of attack. For each simulation the starting location of the vortex was changed so that the minimum passing distance was 4% of the half chord. The paths that the vortex follows for angles of attack 2°, 5°, 10°, and 20° can be seen in Figure 6.17. The response spectrum can be seen in Figure 6.18.

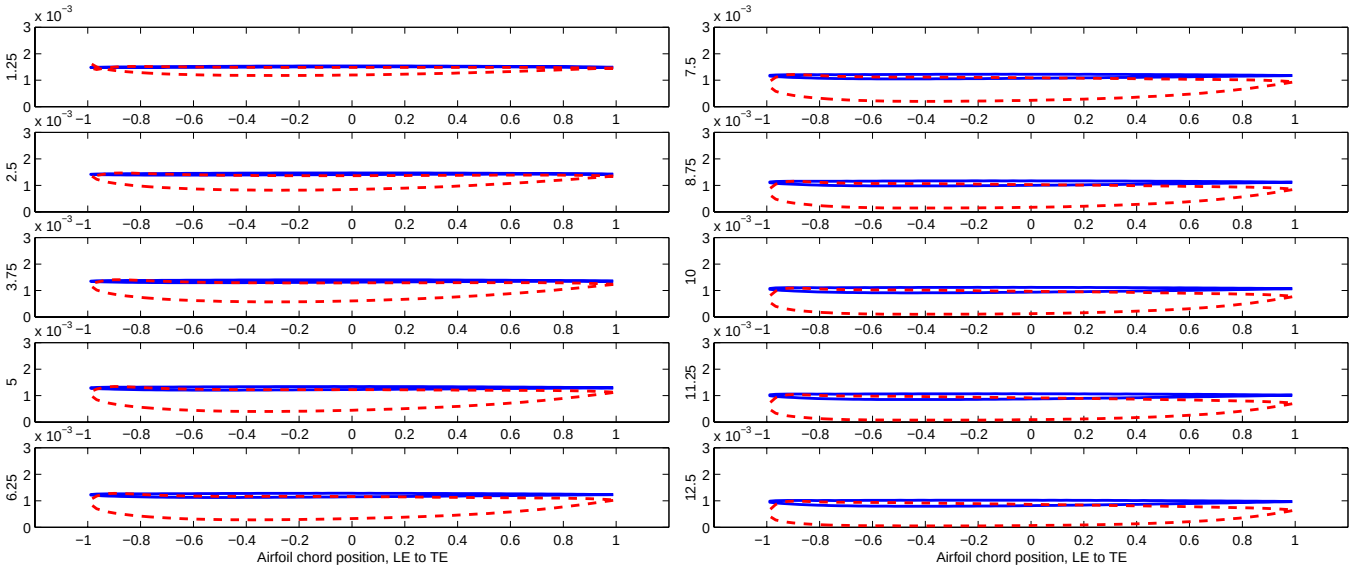

Figure 6.10: Magnitude of induced velocity along the blade section at various normalized frequencies. Flat plate: solid line, NACA 0012: dashed line.

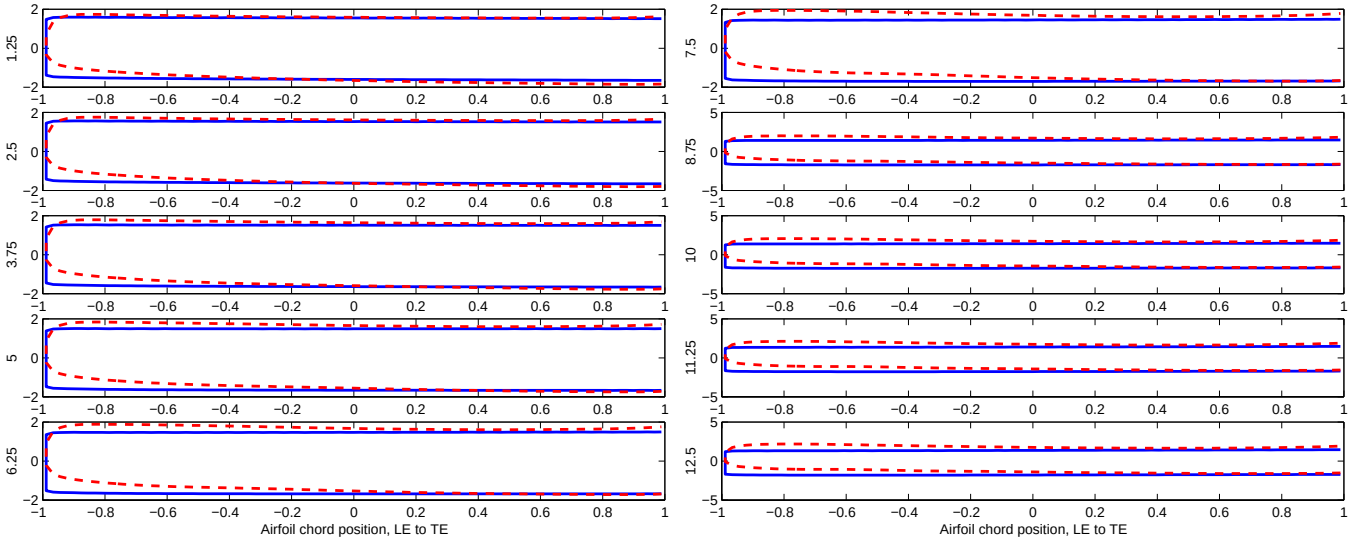

Figure 6.11: Phase * $e^{ik_1 x_1}$ of induced velocity along the blade section at various normalized frequencies. Flat plate: solid line, NACA 0012: dashed line.

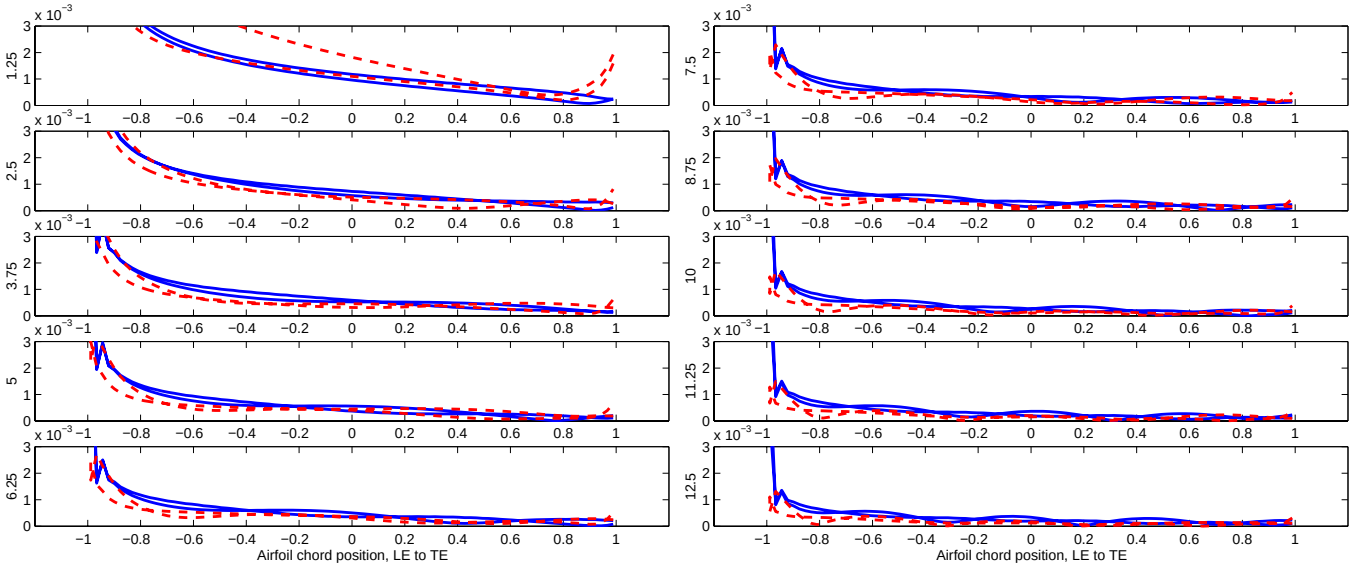

Figure 6.12: Magnitude of the coefficient of pressure along the blade section at various normalized frequencies. Flat plate: solid line, NACA 0012: dashed line.

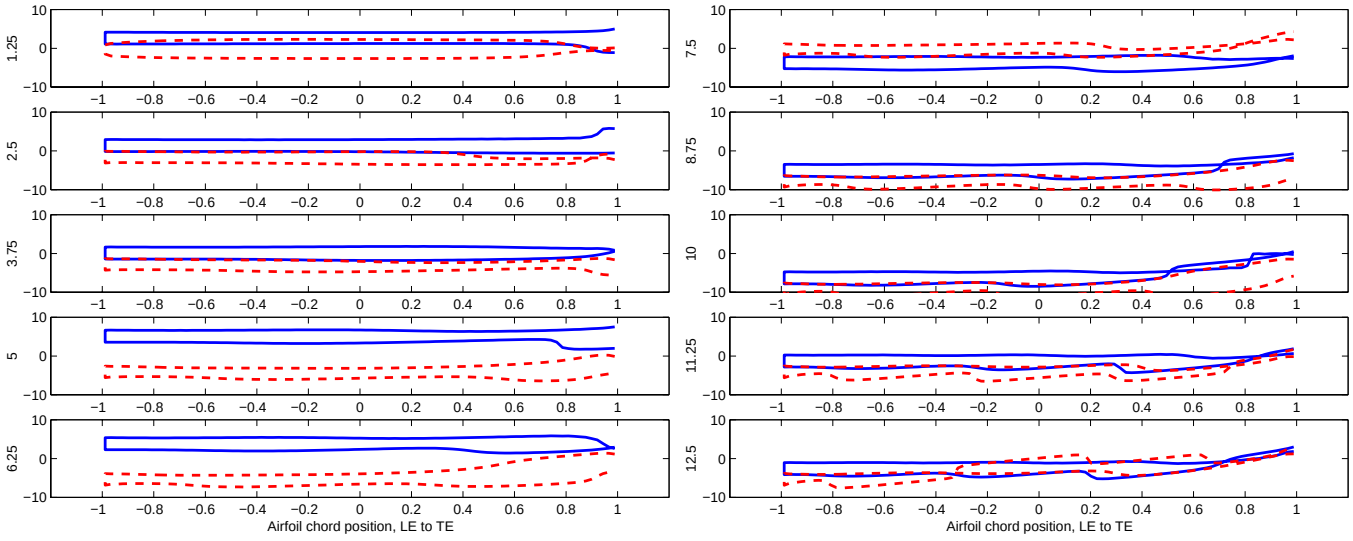

Figure 6.13: Phase of the coefficient of pressure along the blade section at various normalized frequencies. Flat plate: solid line, NACA 0012: dashed line.

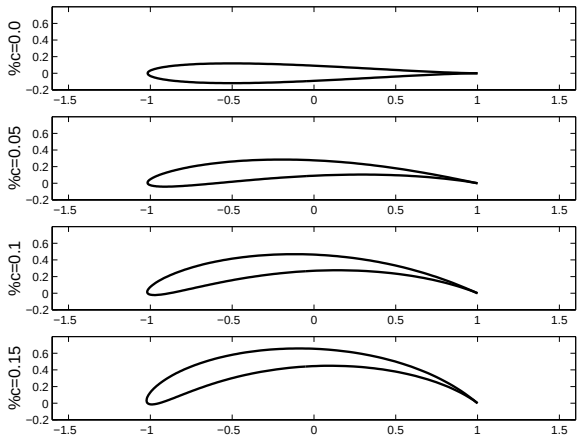

Figure 6.14: Airfoils used in camber simulation.

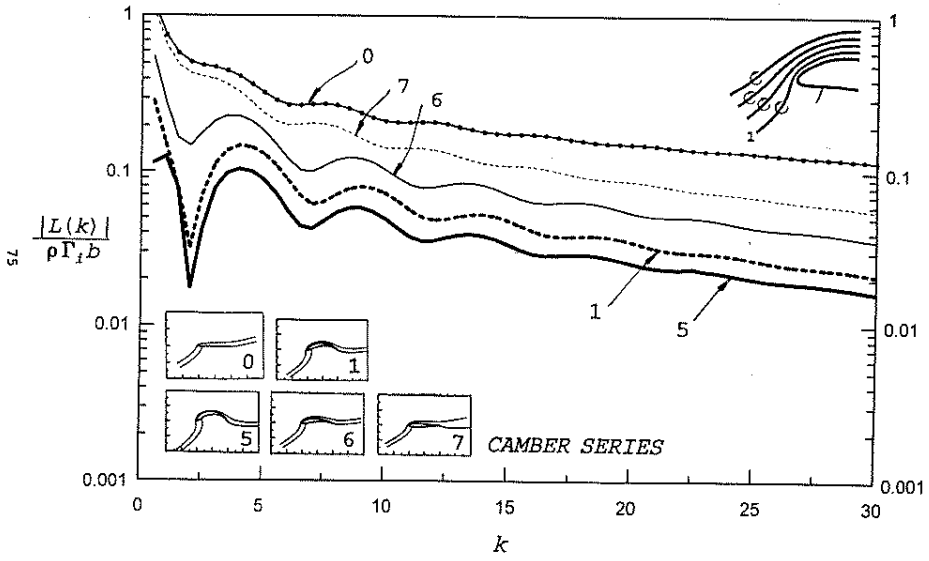

Figure 6.15: Figure 18b from [1].

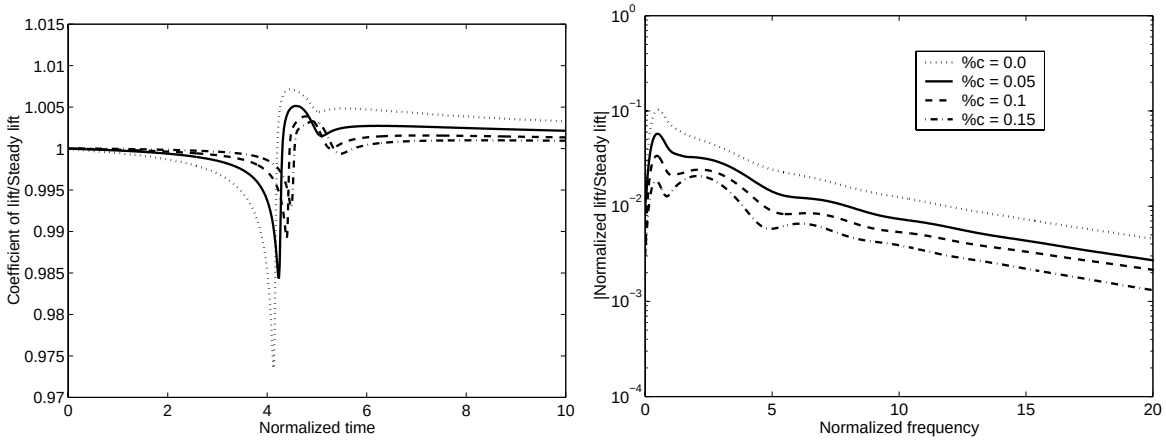

Figure 6.16: Response of the airfoils in time and their associated response spectrum.

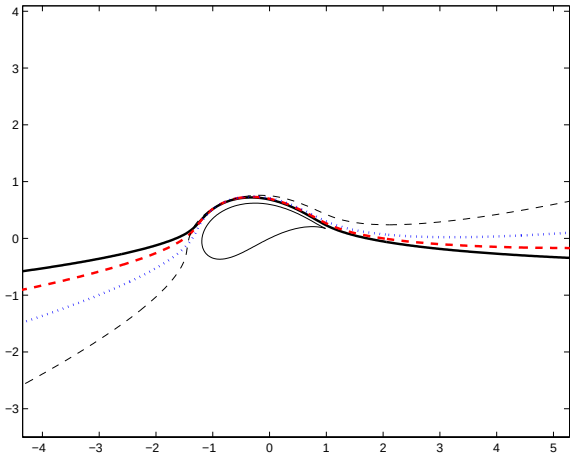

Figure 6.17: Vortex paths for different angles of attack. Joukowski airfoil (Case 3 from [1]). Minimum passing distance kept at 4% of the half chord.

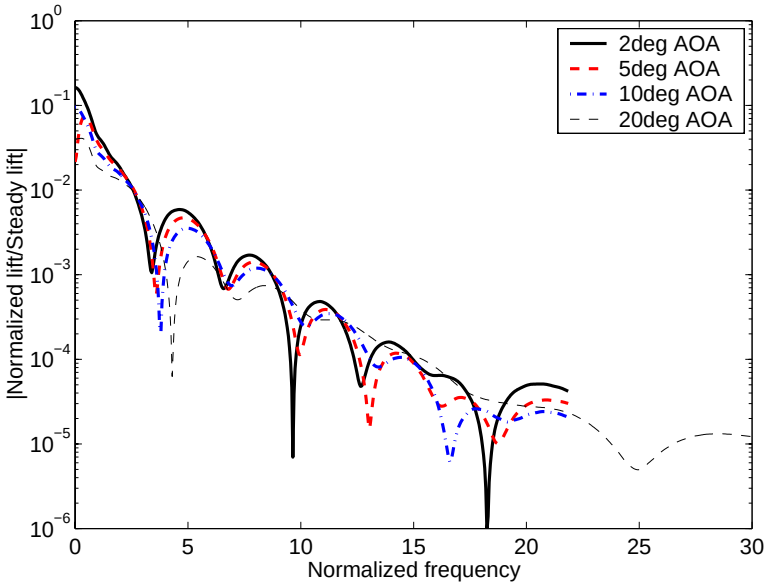

Figure 6.18: Effect of angle of attack on response spectrum

Two of the curves in Figure 6.18 can be compared to prior results. First, the 5° angle of attack case can be compared to the thick solid line in Figure 4.8. In addition, the 20° angle of attack case can be compared to the thick solid line in Figure 4.7. The occurrence of nulls in the spectrum is not consistent between the two methods of prediction. This is not simply a result of the different assumptions. For when calculating the spectrum using the current computational method, but performing an RDT with a vortex strength of 1.0, the occurrence of nulls is related more close to the nulls in Figure 6.18 than to the analytical results. Thus the prediction and justification of the nulls remains an open issue.

7 Geometries of interest to the Navy

This section exemplifies the capability of the current method to treat general blade geometries.

7.1 General interest geometry

A test geometry was supplied in order to preform preliminary calculations on a more realistic blade section shape. The blade section is shown in Figure 7.1. The steady coefficient of lift predicted using the current method with a moderate blade discretization level is 1.0496. When using a convergence criteria to compute the steady lift, the coefficient of lift is predicted to be approximately 1.3. The zero lift angle of attack was computed to be $-5.85°$. If these values are correct, then the unsteady simulations have merit. If they are not, then the grid must be refined until reasonable steady results are obtained. This grid then would be used to compute the unsteady response.

The response of the blade section to a vortex of strength 0.02 passing the blade at various minimum distances is shown in Figures 7.2. The blade section was at an incidence angle of $3°$. It is noted that the coefficient of lift shows a large dip as the vortex passes the trailing edge. This dip is similar to the dip that occurred for the vortex passing the NACA 0012 when the cosine discretization was used. As was shown for the NACA 0012 case, when the lift response in time has a large second dip, the lift spectrum develops prominent scallops. For the geometry of interest in this section, several discretizations were attempted. None removed the the second dip.

7.2 Varying leading edge geometries

Currently, an experiment is being run at David Taylor Model Basin, to characterize inflow and response of blade sections with differing leading edge configurations. Each blade section is tested with the same inflow distortion being created by an upstream square grid of cylindrical rods. The basic blade section shape is a NACA 0012. The other two shapes are formed by replacing the first quarter of the NACA 0012 with different wedge shapes. The leading edge shapes are shown in Figure 7.3. By tapering the leading edge wedge shapes into the quarter chord of the NACA 0012, the overall blade thickness is equivalent for all of the blades.

The response of each blade to the same incident vortex is computed. In the simulation the vortex is introduced at (-4.5, 0.03) and the blade section chord runs from -0.5 to 0.5 along the x-axis. The blades are set at zero incidence. The response in time and the response spectrum can be seen in Figure 7.4. The following observations are made:

- the response is *very* similar for the different shapes
- the blade shape with the sharpest angle gives the lowest overall response at high frequency

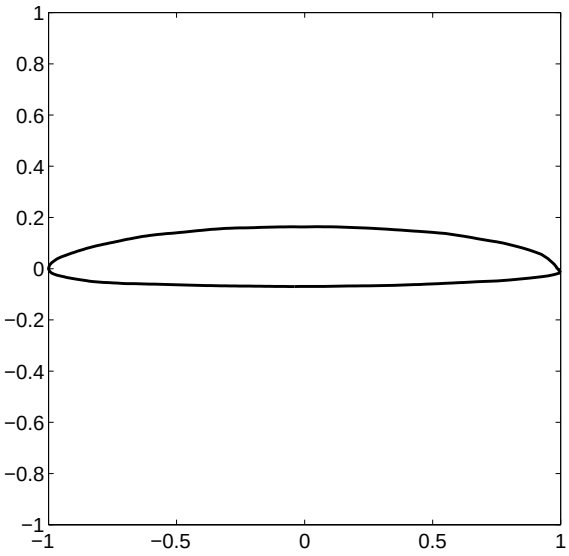

Figure 7.1: Geometry of interest.

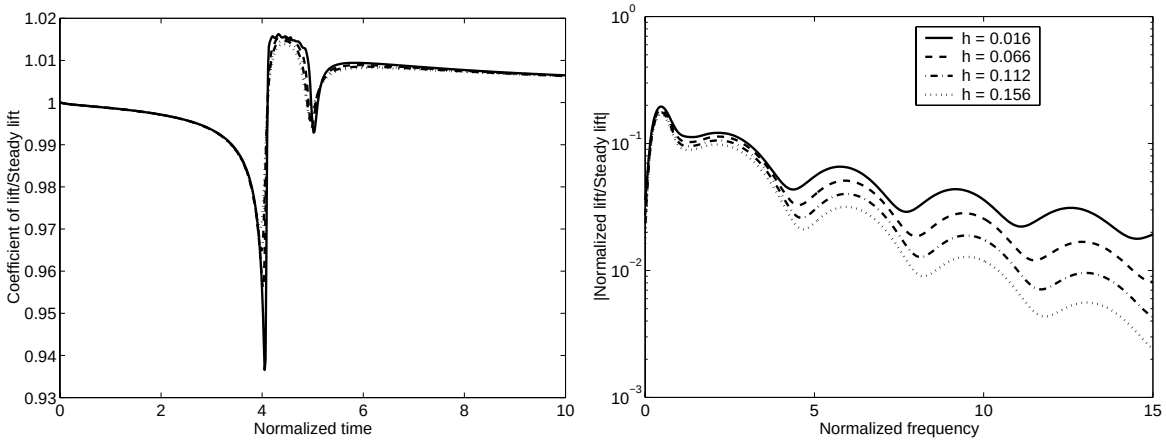

Figure 7.2: Response of general interest geometry to vortices passing with various minimum distances. Response in time (left), response spectrum (right).

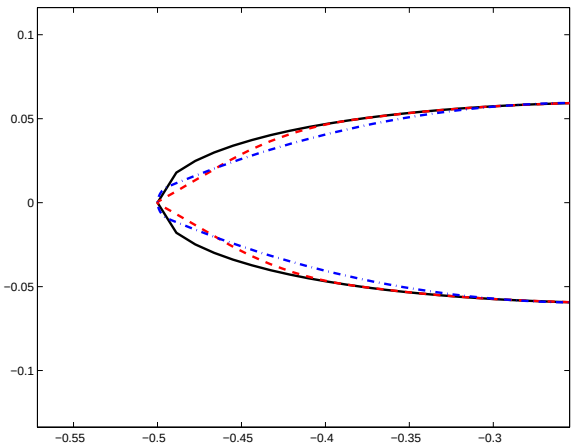

Figure 7.3: Different leading edge geometries under consideration at David Taylor Model Basin.

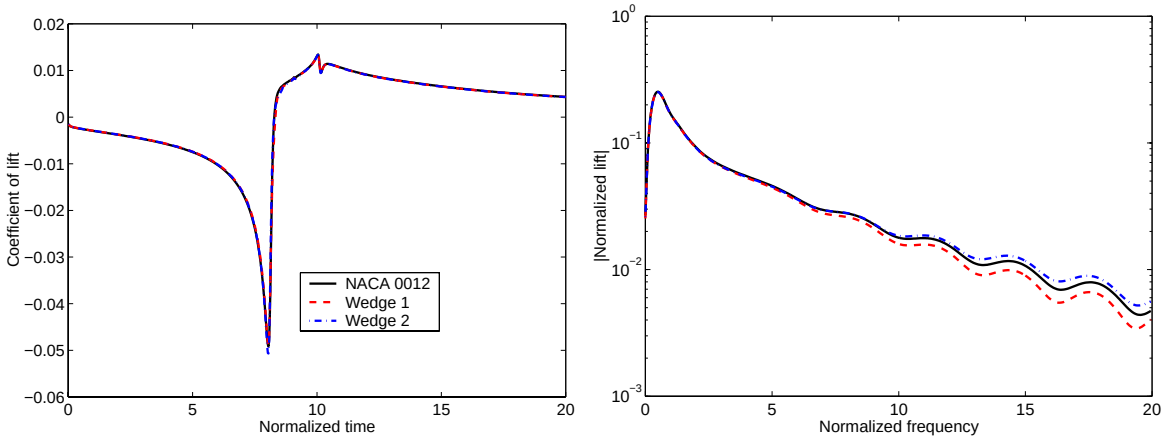

Figure 7.4: Predicted response of different blade section geometries to a vortex passing. Lift vs. time (left), lift vs. frequency (right).

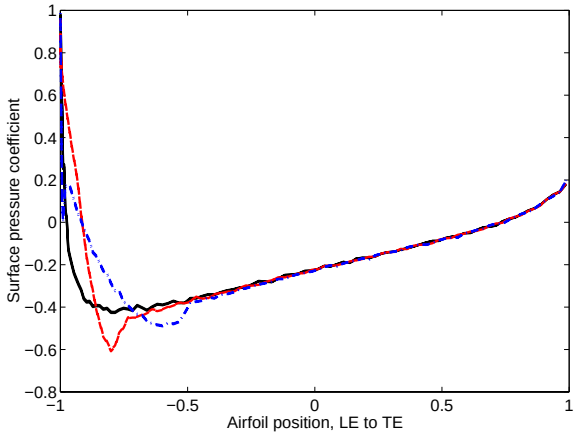

Figure 7.5: Coefficient of pressure for steady flow at no angle of attack past the three airfoil shapes.

A closer look at the steady surface pressure coefficient shows that the leading edge suction for the rounded wedge shape is not what would be expected. The coefficient of pressure for the sharp wedge and the NACA 0012 shown in Figure 7.5 are reasonable; however, they are not smooth. Refining the discretization does not alter the odd behavior. Therefore, it is surmised that the actual geometry description needs to be improved in order to smooth out the pressure predictions.

Because there is a unique opportunity to validate these computations with experimental results. The following sets of curves are presented. Hopefully, surface pressure distributions obtained experimentally can be used to validate these predictions. One possible difficulty for this validation will be the difference between the inflow disturbance that has been modelled and the true inflow disturbance. Figure 7.6 shows the surface pressure distribution for various times. The vortex arrives at the leading edge of the airfoil at $t = 8.0$ and crosses the trailing edge at $t = 10.0$. The time is indicated on the far left of the curves. After the lift builds up during the approach of the vortex, one can see the vortex traveling along the blade by following the small "hiccup" in the surface pressure.

The computations predict the the sharpest wedge shape shows the least response at

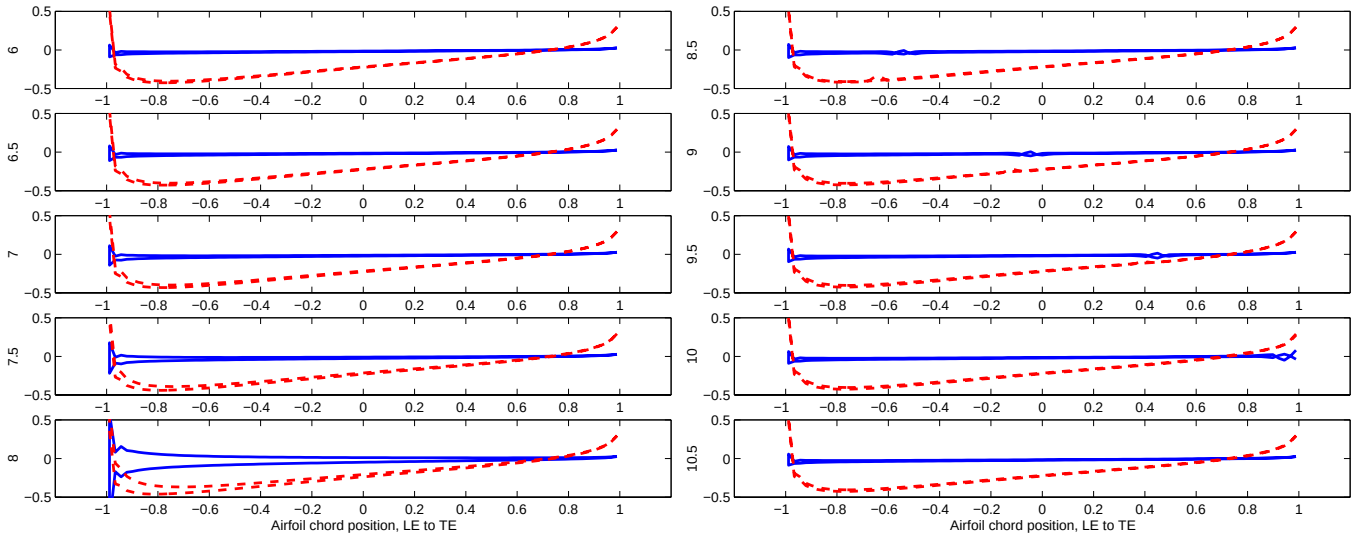

Figure 7.6: Coefficient of pressure along the top and bottom airfoil surfaces. NACA 0001 (solid line), NACA 0012 (dashed line). Time is indicated at the left of the curves.

higher frequencies. This seems to associated with the difference in pressure peak at the leading edge for the different blade section shapes. Figure 7.7 shows the surface pressure coefficient for the three shapes at two different times during the simulation. The first time is approximately when the vortex passes the leading edge and the second time is when the vortex is downstream of the leading edge a bit.

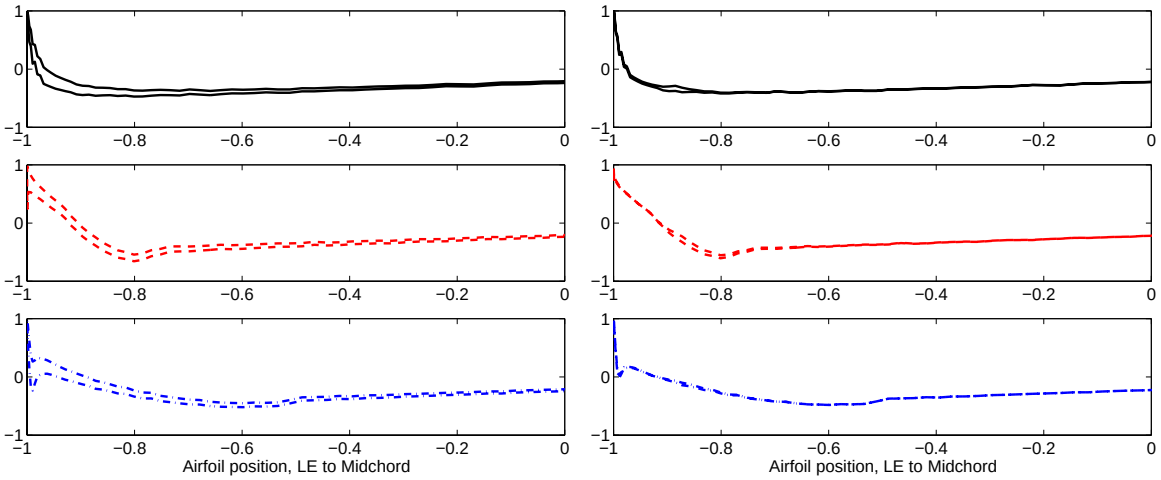

Figure 7.7: Surface pressure coefficient for the NACA 0012 (top), Wedge 1 (middle), Wedge 2 (bottom) at two times. As vortex passes leading edge (left), as vortex moves past the 10% chord location.

8 Other capabilities and possible extensions

8.1 Two-dimensional extensions

The computational capability discussed in this report is flexible. Several different unsteady problems can be run using the BEM technique. In particular, the blade section can be set into an unsteady pitching motion and the response can be calculated. In addition, instead of a single vortex, several vortices, whose initial conditions are either spatially varied or temporarily varied or both can be incident upon the blade section. This feature may allow a more realistic model of turbulence ingestion, as the incident vortices can be calibrated to reflect turbulent parameters of interest.

The acoustic field can also be predicted using this method. Currently, flow field Reynold's stress terms that may contribute to the sound field are not included in the acoustic calculation. However, for the low-speed flows of interest to the navy, neglecting this effect should not affect the acoustic prediction greatly. As an example of this capability, the pressure at the fly over point for the flat plate and the NACA 0012 airfoil is calculated in the midfield and in the far field. See Figure 8.1. The value for the coefficient of pressure at the fly over point for the NACA 0012 in the very far field is so small that large errors are introduced when computing the Fourier transform. Thus, the reported far field pressure at frequencies higher than 6 (for the NACA 0012 case) should be ignored. By studying the pressure directivity in the mid and far fields for two fixed frequencies, the importance of the second wave number can be seen. Figure 8.2 shows the directivity at a reduced frequency of 1.0. At this frequency the flat plate and NACA 0012 foil radiation is almost identical. However, at a reduced frequency of 3.0, shown in Figure 8.3, the far field response shows the impact of a longitudinal disturbance on the thicker foil.

8.2 Extension to three dimensions

A very different extension of this work would be to observe finite span effects by using the three-dimensional version of this code. The free-wake evolution in the three-dimensional code leads to the formation of tip vortices as shown in Figure 8.4. The unsteady capabilities of the three dimensional code have already been validated by considering results for the limit of very large aspect ratio. The results from this validation are reported in a conference paper written for the upcoming ASME IMECE to be held in November, 2000, in Orlando, Florida. A copy of this conference paper is included as Appendix C. Also included in the conference paper are validations for the computed three-dimensional acoustic field.

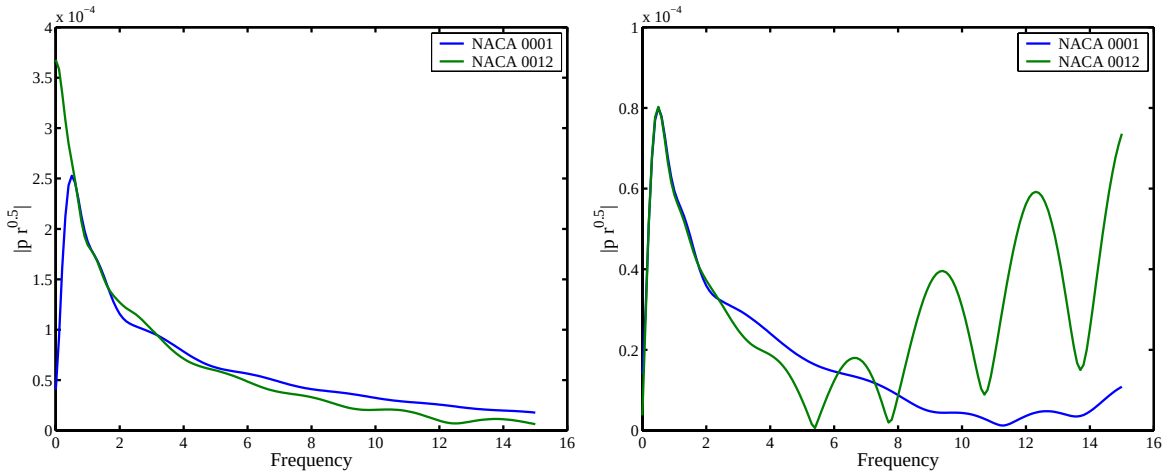

Figure 8.1: Coefficient of pressure vs. frequency at flyover position. 10 chords away (left), 100 chords away (right).

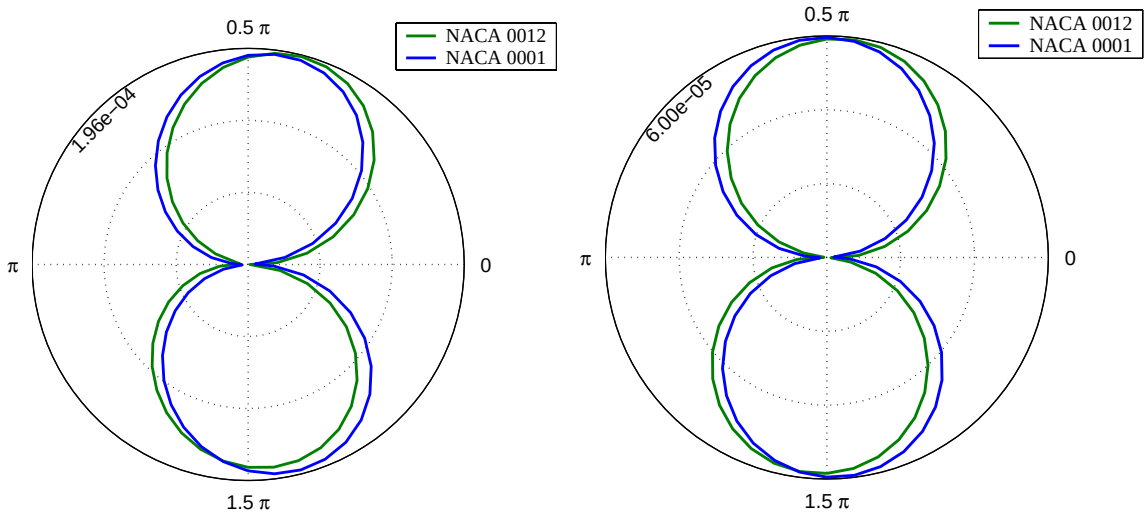

Figure 8.2: Directivity of the coefficient of pressure at normalized frequency of 1.0. On circular arc 10 chords away (left) and 100 chords away (right).

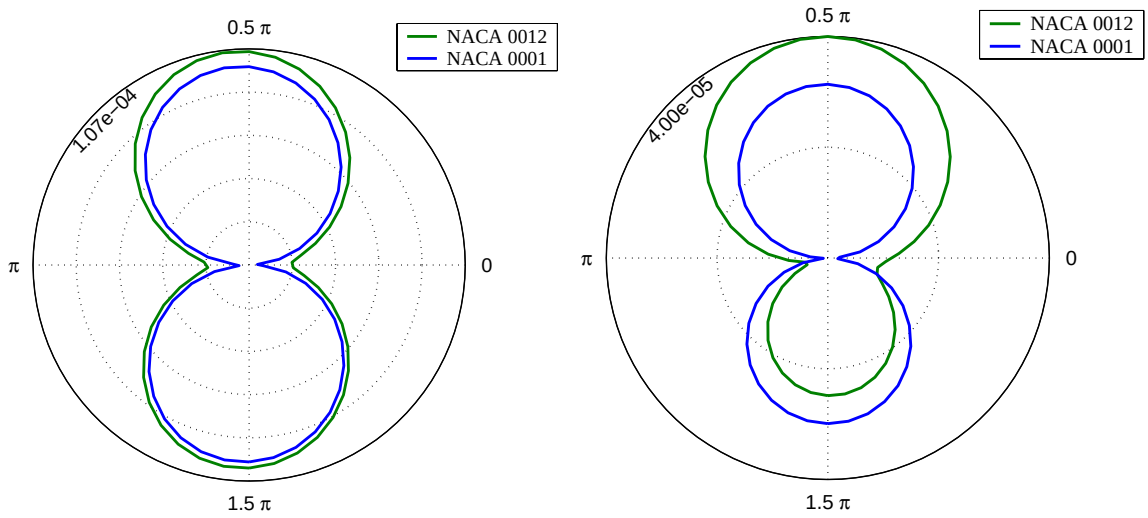

Figure 8.3: Directivity of the coefficient of pressure at normalized frequency of 3.0. On circular arc 10 chords away (left) and 100 chords away (right).

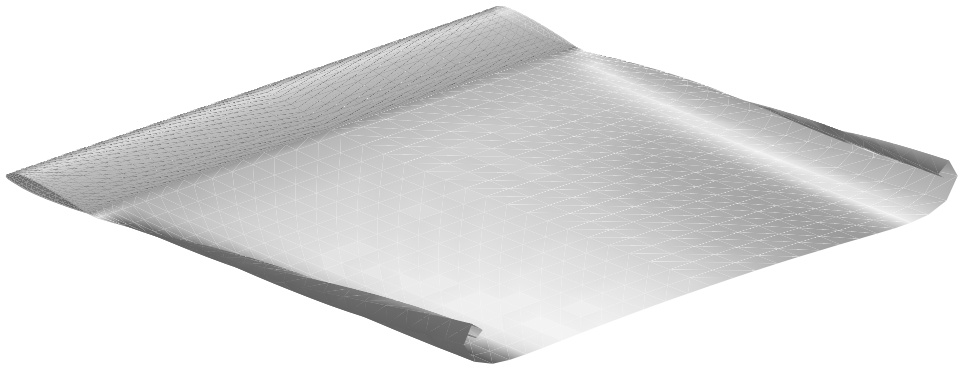

Figure 8.4: A view of a typical wake shape at steady-state (Aspect ratio of 6). Reproduced from ref. 10.

Bibliography

[1] Martinez, R., Rudzinsky, J., and Atassi, H. M., "Analytic Evaluation of Shape Effects on Blade-Vortex Interaction," Tech. Rep. U-2466-402.14, Cambridge Acoustical Associates, Dec. 1997.

[2] Howe, M. S., *Acoustics of Fluid-Structure Interactions*, chap. 3, Cambridge Press, 1998, p. 189.

[3] Morino, L., "A General Thoery of Unsteady Compressible Potential Aerodynamics," Tech. Rep. CR-2464, NASA, 1973.

[4] Gennaretti, M., Luceri, L., and Morino, L., "A Unified Boundary Integral Methodology for Aerodynamics and Aeroacoustics of Rotors," *J. Sound and Vib.*, Vol. 200, No. 4, 1997, pp. 467–89.

[5] Morino, L., "Boundary Integral Equations In Aerodynamics," *Appl. Mech. Rev.*, Vol. 46, No. 8, 1993, pp. 445–66.

[6] Morino, L. and Tseng, K., "Steady, Oscillatory and Unsteady, Subsonic and Supersonic Aerodynamics (SOUSSA) For Complex Airfcraft Configurations," *Unsteady Aerodynamics*, 1977, AGARD CP-273.

[7] Wood, T. H. and Grace, S. M., "Free-Wake Analysis for Calculating the Aeroacoustics of a Wing-Flap Configuration," *Proceedings of the 38th AIAA Aerospace Sciences Meeting*, Reno, NV, Jan 10-13 2000, pp. 162–173, Paper no. AIAA 2000-0607.

[8] Ramsey, W. D., *Boundary integral methods for Lifting Bodies with Vortex Wakes*, Ph.D. thesis, Massachusetts Institute of Technology, Cambridge, Massachusetts, 1996.

[9] Rule, J. A., Epstein, R. J., and Bliss, D. B., "An Analytical/Numerical Matching - Turbulent Core Model Blade Vortex Interaction Study," *Paper 97-1707-CP*, 1997.

[10] Wood, T. H., "Aeroacoustic Predictions of a High-lift Wing Configuration in Three Dimensions," Tech. Rep. PhD Prospectus, Boston University, August 1999.

[11] Lighthill, M. J., "On Displacement Thickness," *Journal of Fluid Mechanics*, Vol. 4, 1958, pp. 383–92.

[12] Crighton, D. G., "The Kutta Condition in Unsteady Flow," *Ann. Rev. Fluid Mech.*, Vol. 17, 1985, pp. 411–45.

[13] Goldstein, M. E., *Aeroacoustics*, McGraw-Hill International Book Co., New York, etc., 1976.

[14] Morino, L., Chen, L.-T., and Suciu, E., "Steady and Oscillatory Subsonic and Supersonic Aerodynamics around Complex Configurations," *AIAA J.*, Vol. 13, No. 3, 1975, pp. 368–374.

[15] Tseng, K., *Nonlinear Green's Function Method for Transonic Potential Flow*, Ph.D. thesis, Boston University, Boston, Massachusetts, 1983.

[16] Katz, J. and Plotkin, A., *Low-Speed Aerodynamics*, McGraw-Hill, Inc., New York, etc., 1991.

[17] Krasny, R., "Desingularization of Periodic Vortex Sheet Roll-Up," *Journal of Computational Physics*, Vol. 65, 1986, pp. 292–313.

[18] Hess, J. L. and Smith, A. M. O., "Calculation of Potential Flow About Arbitrary Bodies," *Prog. in Aeronautical Sciences*, Vol. 8, 1967.

A Derivation of equations of motion and BEM governing equations

This appendix is adapted from the PhD thesis prospectus of Trevor H. Wood, research assistant in the Deparment of Aerospace and Mechanical engineering at Boston University.[10]

Nomenclature

$\rho, \mathbf{v}, p, s, h$	fluid density, velocity, pressure, specific entropy, and specific enthalpy
$\frac{D}{Dt} = \frac{\partial}{\partial t} + \mathbf{v} \cdot \nabla$	material derivative
$\frac{D_o}{Dt} = \frac{\partial}{\partial t} + U_\infty \frac{\partial}{\partial x_1}$	linearized material derivative
c	speed of sound
M	Mach number
L	length scale (approx. 777 chord)
Φ, ϕ	total, perturbation velocity potential
σ	homogeneous (non-linear source) terms
$H(x)$	Heaviside step function
β	Prandtl-Glauert parameter
δ	flap deflection angle
$\theta = \cos^{-1}(\mathbf{n} \cdot \hat{r})$	observer declination angle
C_P	coefficient of pressure
I, P	acoustic intensity, power
$\mathcal{P}$	power level
γ	ratio of specific heats
ξ	vorticity vector
,	circulation
$\delta(x)$	Dirac delta function
δ_{ij}	Kronecker delta tensor
ϵ_{ijk}	antisymmetric permutation tensor
$\tau^\star = t - \Theta$	retardation time
$\Theta = m + \alpha$	retardation time delay, $m \equiv$integer part
ϵ	regularization parameter
∂_x	partial derivative with respect to x
$\mathbf{n}$	outward unit normal vector
$(\mathbf{x}, t), (\mathbf{y}, \tau)$	source, observer position and time
$\hat{\mathbf{r}}$	radial unit vector (source to observer)
S	smooth surface S
V	fluid volume outside S
f	surface generating function
$\mathcal{L}$	self-adjoint linear differential operator
$\mathcal{F}$	surface sources
G	Green's function

Subscripts:		**Superscripts:**		**Overscripts:**	
∞	undisturbed value	$\prime$	derivative wrt argument	$\tilde{}$	Prandtl-Glauert space
i	i^{th} spatial coordinate	(B)	solid body part	$\dot{}$	time derivative
t	time derivative	(W)	wake part	$\hat{}$	unit vector
x_i	spatial derivative along x_i	$+,-$	above, below ($\pm\mathbf{n}$) wake		
(TE)	panel adjacent to trailing edge				

A.1 Potential flow equations

We consider fluid flowing past a streamlined body at high Reynolds numbers and subsonic velocities. The first order solution to the equations of conservation of fluid mass and momentum satisfies the inviscid Euler equations with additional conditions describing the generation of thin shear layers at sharp edges of the solid bodies. If the fluid disturbances are assumed to be adiabatic and the specific heats are taken to be constant, then the flow may be described by the velocity potential everywhere in the fluid except in the thin regions of the wakes and boundary layers. In these regions, vorticity is introduced to effect steep gradients, or jumps, in the fluid velocity. Such a flow is often referred to as *quasi-potential* flow in the literature because the vorticity exists only in very localized regions.[5] For a review of compressible potential flow, see Appendix A.3. In the potential flow regions, the inviscid Euler equations take the form of a wave equation, Eq. (A.52),

$$\nabla^2\Phi - \frac{1}{c_\infty^2}\frac{\partial^2\Phi}{\partial t^2} = -\sigma_1 = \frac{1}{c_\infty^2}\left[(c_\infty^2 - c^2)\nabla^2\Phi + 2\mathbf{v}\cdot\frac{\partial\mathbf{v}}{\partial t} + \frac{\mathbf{v}}{2}\cdot\nabla v^2\right], \tag{A.1}$$

where $\mathbf{v} = \nabla\Phi$ and the reference frame is motionless with respect to the undisturbed fluid. If the wing is assumed to move at a constant velocity, $-U_\infty\hat{i}$, the *perturbation potential*, $\phi = \Phi - U_\infty x_1$ satisfies the above equation when the time derivatives are replaced by the freestream material derivative,

$$\frac{D_o}{Dt} = \frac{\partial}{\partial t} + U_\infty\frac{\partial}{\partial x_1}. \tag{A.2}$$

Here, the frame of reference moves with the wing. Nondimensionalizing space and time by the characteristic dimensions L and L/U_∞, respectively, gives

$$\nabla^2\phi - M_\infty^2\frac{{D_o}^2\phi}{Dt^2} = -\sigma = \frac{c_\infty^2 - c^2}{c_\infty^2}\nabla^2\phi + 2M_\infty^2\mathbf{v}\cdot\frac{D_o\mathbf{v}}{Dt} + \frac{M_\infty^2\mathbf{v}}{2}\cdot\nabla v^2. \tag{A.3}$$

By using the Prandtl-Glauert transformation,

$$\left\{\tilde{x}_1, \tilde{x}_2, \tilde{x}_3, \tilde{t}\right\} = \left\{\frac{x_1}{\beta}, x_2, x_3, t - \frac{x_1}{\tilde{c}^2}\right\}, \tag{A.4}$$

the wave equation takes a classical diagonal form, shown in Eq. (A.96), for which the corresponding boundary integral equation is given by,

$$4\pi H(f)\phi(\mathbf{x},t) = \int_V \left[\frac{\tilde{\sigma}}{r_\beta}\right]_{\tau^\star} dV - \int_S \frac{1}{r_\beta\sqrt{1 - M^2n_1^2}}\times \tag{A.5}$$
$$\left[\left(1 - M^2n_1^2\right)\frac{\partial\phi}{\partial n} + \frac{\cos\theta}{r_\beta}\phi + \left(\frac{\cos\theta}{\beta} - Mn_1\right)M\dot{\phi} - M^2n_1\sqrt{1 - n_1^2}\frac{\partial\phi}{\partial t_1}\right]_{\tau^\star}\frac{dS}{\beta},$$

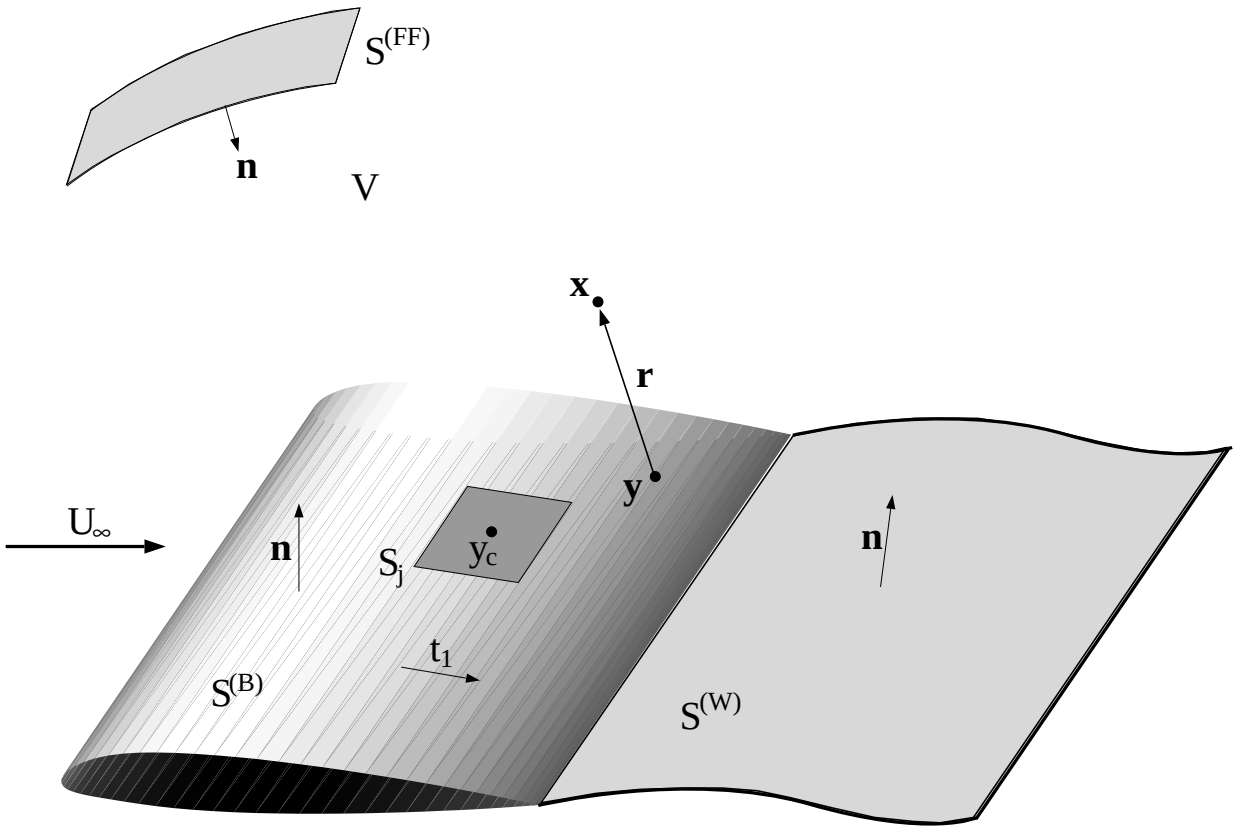

Figure A.1: Definitions of boundary integral quantities

(Eq. (A.112) in the Appendix) where $\cos\theta = \hat{r} \cdot \mathbf{n}$,

$$\tau^\star = t - \frac{M}{\beta}\left(r_\beta - \frac{Mx_1}{\beta^2}\right) \tag{A.6}$$

$$r_\beta(\mathbf{x}|\mathbf{y}) = \sqrt{(x_1-y_1)^2/\beta^2 + (x_2-y_2)^2 + (x_3-y_3)^2}, \tag{A.7}$$

and $\partial/\partial t_1$ is the gradient along a tangent to the surface lying parallel to the $x_2 - x_3$ plane. The near-field surface of the integration envelops the wing and wakes such that the normal to the surface points into the fluid (see Figure A.1). For infinitely thin wakes, the wake integrals reduce to the integral of the jump in the integrand (from upper to lower surface) along the upper portion of $S^{(W)}$. See Appendix A.3.2 for details on boundary integral methods and the derivation of Equation (A.5).

For the current application the Mach numbers are typically in the low subsonic range and, thus, the nonlinear source terms, σ, will be initially neglected. Equation (A.5) then expresses the perturbation velocity potential in terms of monopole (source) and dipole (doublet) sources distributed along the boundaries. Assuming that the disturbances are outgoing in the acoustic far field and are zero infinitely far away from the wing, the surface integrals in Eq. (A.5) reduce to integrals over the surfaces of the wing and around the wakes (i.e., $S^{(FF)}$ does not contribute).

The impermeability condition is applied at the solid surfaces such that the fluid velocity normal to the surface is equal to the normal velocity of the surface. Note that the effects

of finite boundary layer thickness may be taken into account by including a *transpiration velocity* through the surface to essentially place the surface separating potential and viscous flow regimes at the momentum boundary layer thickness.[11] However, this will not be included in the initial investigations as it is believed that the sound radiation will not be significantly affected. In contrast, the shear layer dynamics is expected to provide the mechanisms for the dominant sources of sound radiation. For the thin shear layer model of the wakes, the integrand reduces to its jump across the surface of the shear layer. The normal derivative is continuous across an infinitely thin wake and the potential jump is approximately constant in time (in the Lagrangian frame) for very long time scales of viscous diffusion. The potential jump is determined using the Kutta condition which essentially states that the flow velocity must remain finite at the trailing edge.[12]

With the stated boundary conditions and a given initial condition, Eq. (A.5) must be solved numerically when arbitrary surface geometries are of interest. This numerical solution is discussed further in the following chapter. Once the surface sources are determined, Eq. (A.5) may be evaluated directly to determine the velocity potential in the field. Similarly, the velocity field may be determined by taking the gradient of Eq. (A.5) in the $\mathbf{x}$ domain and integrating directly. The field pressure may then be evaluated using Bernoulli's Equation (A.60)

$$C_p = \frac{p - p_\infty}{\frac{1}{2}\rho_\infty U^2} = \frac{p_\infty}{\frac{1}{2}\rho_\infty U^2}\left[\left(1 - \frac{\dot{\phi} + \frac{v^2}{2}}{h_\infty}\right)^{\frac{\gamma}{\gamma-1}} - 1\right]. \tag{A.8}$$

The acoustic intensity is given in dimensionless form by[13]

$$\mathbf{I} = (p' + 2\mathbf{v}' \cdot \mathbf{v}_o)\left(\mathbf{v}' + \frac{1}{2}\gamma M^2 p' \mathbf{v}_o\right), \tag{A.9}$$

where primes and zero subscripts denote time-varying and steady contributions, respectively. Note that the intensity is scaled by $\rho_o U_\infty^3/2$ and the acoustic density relates to the pressure in dimensionless form by $\rho' = \gamma M^2 p'/2$ for adiabatic disturbances.

A.2 Numerical Solution

Equation (A.5) is an integro-differential-delay equation for the perturbation potential ϕ. By integrating numerically in time from a set initial condition, the potential may be calculated at each time-step using a *boundary element method*. In this research, a first order geometric discretization and zeroth order field discretization method will be used for simplicity. This formulation was used in the panel code SOUSSA, and the ensuing details in this section follow those of [Ref. 14, 15]. The solid surfaces and wakes are divided into N and N_W hyperboloidal panels (see eqs. (A.121) and (A.122) in Appendix A.3.3), respectively, over which the unknowns ϕ_j $(j = 1, N + N_W)$ are assumed constant. Under this assumption, the boundary integral equation (A.5) takes the form

$$\begin{aligned} 2\pi\beta\phi_i(t) &= \sum_j^N \left[G^{(B)}_{D_{ij}}\phi_j(t) - G_{S_{ij}}\left(\frac{\partial\phi(t)}{\partial n}\right)_j + G_{T_{ij}}\dot{\phi}(t)_j + G_{G_{ij}}\left(\frac{\partial\phi(t)}{\partial t_1}\right)_j \right]_{\tau^\star} \\ &+ \sum_j^{N_W} \left[G^{(W)}_{D_{ij}}\Delta\phi_j(t) \right]_{\tau^\star}, \end{aligned} \tag{A.10}$$

where B and W refer to the solid bodies and wakes, respectively, and

$$\begin{aligned} G_{D_{ij}} &= -\frac{1}{\sqrt{1-M^2n_1^2}}\int_{S_j}\frac{\cos\theta}{r^2_\beta(\mathbf{x}_i|\mathbf{y})}dS, \\ G_{S_{ij}} &= \sqrt{1-M^2n_1^2}\int_{S_j}\frac{1}{r_\beta(\mathbf{x}_i|\mathbf{y})}dS, \\ G_{T_{ij}} &= -\frac{M}{\sqrt{1-M^2n_1^2}}\int_{S_j}\left[\frac{\cos\theta/\beta - Mn_1}{r_\beta(\mathbf{x}_i|\mathbf{y})}\right]dS \simeq \frac{Mr_\beta}{\beta}G_{D_{ij}} + \frac{M^2n_1}{1-M^2n_1^2}G_{S_{ij}}, \\ G_{G_{ij}} &= \frac{M^2n_1\sqrt{1-n_1^2}}{\sqrt{1-M^2n_1^2}}\int_{S_j}\frac{1}{r_\beta(\mathbf{x}_i|\mathbf{y})}dS. \end{aligned} \tag{A.11}$$

For low subsonic Mach numbers, $M \ll 1$, the G_G term and the second term of G_T are of $\mathcal{O}(M^2)$ and may be neglected. The doublet and source influences may be evaluated analytically for hyperboloidal panels that are approximately flat and are given in equations (A.124)–(A.126).

Equation (A.10) may be integrated numerically in time by assuming linear interpolation between the temporal data $\phi_i^k = \phi_i(t = k\Delta t)$. The time delay $\Theta = t - \tau_\star$ is now written separately as

$$\Theta_{ij} = m_{ij} + \alpha_{ij} = \frac{M}{\beta}\left(r_{\beta_{ij}} - \frac{Mx_{1_i}}{\beta}\right), \tag{A.12}$$

where m_{ij} is an integer, $\alpha_{ij} \in [0, 1)$ is real, and $r_{\beta_{ij}} = r_\beta(\mathbf{x}_i|\mathbf{y}_{c_j})$ ($\mathbf{y}_{c_j}$ locates the center of the j$^{\text{th}}$ panel). To approximate the time derivative of the potential, a first order backward discretization will be used. Defining m'_{ij} and α'_{ij} such that

$$\Theta_{ij} + \Delta t = m'_{ij} + \alpha'_{ij}, \tag{A.13}$$

the unknown field data may now be expressed by

$$\begin{aligned}
\phi_j^k &= (1-\alpha_{ij})\phi_j^{k-m_{ij}} + \alpha_{ij}\phi_j^{k-m_{ij}-1}, \\
\left(\frac{\partial\phi}{\partial n}\right)_j^k &= (1-\alpha_{ij})\left(\frac{\partial\phi}{\partial n}\right)_j^{k-m_{ij}} + \alpha_{ij}\left(\frac{\partial\phi}{\partial n}\right)_j^{k-m_{ij}-1}, \\
\dot{\phi}_j^k &= \left[\left((1-\alpha_{ij})\phi_j^{k-m_{ij}} + \alpha_{ij}\phi_j^{k-m_{ij}-1}\right)\right. \\
&- \left.\left((1-\alpha'_{ij})\phi_j^{k-m'_{ij}} + \alpha'_{ij}\phi_j^{k-m'_{ij}-1}\right)\right]\frac{1}{\Delta t},
\end{aligned} \tag{A.14}$$

where first-order backward differencing is used to approximate the temporal derivatives.

The discretized equations become finally

$$\begin{aligned}
2\pi\beta\phi_i^k &= \left(G_{D_{ij}}^{(B)} + G_{T_{ij}}/\Delta t\right)\left[(1-\alpha_{ij})\phi_j^{k-m_{ij}} + \alpha_{ij}\phi_j^{k-m_{ij}-1}\right] \\
&- G_{S_{ij}}\left[(1-\alpha_{ij})\left(\frac{\partial\phi}{\partial n}\right)_j^{k-m_{ij}} + \alpha_{ij}\left(\frac{\partial\phi}{\partial n}\right)_j^{k-m_{ij}-1}\right] \\
&- G_{T_{ij}}\left[(1-\alpha'_{ij})\dot{\phi}_j^{k-m'_{ij}} + \alpha'_{ij}\dot{\phi}_j^{k-m'_{ij}-1}\right]/\Delta t \\
&+ G_{D_{ij}}^{(W)}\left[(1-\alpha_{ij})\Delta\phi_j^{k-m_{ij}} + \alpha_{ij}\Delta\phi_j^{k-m_{ij}-1}\right]
\end{aligned} \tag{A.15}$$

where summation is assumed over repeated indices. By applying this equation at N collocation points located at the centers of the N panels on the solid bodies, the impermeability condition on the solid surface boundaries

$$\frac{\partial\phi}{\partial n} = -\mathbf{n}\cdot\hat{i}, \tag{A.16}$$

and the Kutta condition at the trailing edges,

$$\Delta\phi_{(TE)}^{(W)} = \phi_{(TE^+)}^{(B)} - \phi_{(TE^-)}^{(B)}, \tag{A.17}$$

this equation may be solved for the unknown potential at the latest time-step. The Kutta condition ensures that there is no concentrated vortex at the sharp trailing edges by setting the potential jump of the adjacent wake panels to cancel that of the adjacent surface panels. The wakes are then evolved forward in time through the numerical integration of

$$\frac{d\mathbf{x}_\star}{dt} = \mathbf{v}_\star \tag{A.18}$$

where $\mathbf{x}_\star$ represents the corners of the wake panels and $\mathbf{v}_\star$ is the local fluid velocity at $\mathbf{x}_\star$. A simple Euler forward numerical integration of Eq. (A.18) is currently used, and is described in further detail in the following section.

Equations (A.15) include leading order compressibility effects. The preliminary results presented in this prospectus will neglect compressibility to simplify the code development and validation process. For incompressible flows, these equations reduce to

$$\left(2\pi\delta_{ij} - G_{D_{ij}}^{(B)}\right)\phi_j^k = -G_{S_{ij}}\left(\frac{\partial\phi}{\partial n}\right)_j^k + G_{D_{ij}}^{(W)}\Delta\phi_j^k. \tag{A.19}$$

The far-field evaluation of the acoustic pressure (A.8) and intensity (A.9) also reduce to the following

$$C_p = -2\left(\dot{\phi} - \frac{\partial \phi}{\partial x_1}\right), \tag{A.20}$$

$$\mathbf{I} = \left(C_p + 2\frac{\partial \phi}{\partial x_1}\right)\nabla\phi, \tag{A.21}$$

to leading order in the perturbation velocity.

A.2.1 Wake Evolution

The wakes are composed of doublet panels with a constant strength, $\Delta\phi$, determined using the Kutta condition. The influence of a constant strength doublet panel is mathematically equivalent to that of a vortex ring. The wakes are thus modelled as thin vortex sheets that evolve freely with the local flowfield. An accurate wake evolution is important if potential feedback mechanisms and acoustic sources are to be simulated.

The wake dynamics are governed by the equations of mass and momentum conservation. When applied to a control surface surrounding and moving with the wake, these give

$$\frac{d}{dt}\int_V \rho\, dV = -\int_S \rho \mathbf{v}_{\rm rel}\cdot\mathbf{n}\, dS \tag{A.22}$$

$$\frac{d}{dt}\int_V \rho\mathbf{v}\, dV = -\int_S \left[\mathbf{v}_{\rm rel}\rho\mathbf{v}\cdot\mathbf{n} + p\mathbf{n}\right] dS \tag{A.23}$$

where $\mathbf{n}$ is the unit vector normal to the wake surface and $\mathbf{v}_{\rm rel}$ is the relative velocity through the surface S. When the thickness of the wake is taken to be infinitesimally small, the volume integrals above give zero. It follows that the jump of the integrands of the surface integrals must be zero; i.e.,

$$\Delta\left[\rho(v_n - v_w)\right] = 0, \tag{A.24}$$

$$\Delta\left[\rho(v_n - v_w)\mathbf{v} + p\mathbf{n}\right] = 0,, \tag{A.25}$$

where v_w is the normal velocity of the wake surface and $v_n = \mathbf{v}\cdot\mathbf{n}$. If the incompressible flow limit is initially assumed, Eq. (A.24) implies

$$\Delta\left(\frac{\partial\phi}{\partial n}\right) = 0; \tag{A.26}$$

i.e., the monopole source strength of infinitesimally thin wakes is zero. Eq. (A.25) gives conditions for both the normal and tangential components of the equation. The normal components give

$$\Delta p = 0, \tag{A.27}$$

and the tangential components give $\rho(v_n - v_w)\Delta\mathbf{v} = 0$ which, for nontrivial velocity jumps, implies impermeability,

$$v_n = v_w. \tag{A.28}$$

Consider the incompressible Bernoulli's equation,

$$\frac{\Delta p}{\rho} + \Delta\left(\frac{v^2}{2}\right) + \Delta\dot{\phi} = 0. \tag{A.29}$$

By applying the condition of pressure continuity, Eq. (A.27), Bernoulli's equation gives an important relation:

$$\Delta\dot{\phi} + \frac{1}{2}(\mathbf{v}^+ + \mathbf{v}^-)\cdot(\Delta\mathbf{v}) = \frac{D_w}{Dt}\Delta\phi = 0, \tag{A.30}$$

where

$$\frac{D_w}{Dt} = \frac{\partial}{\partial t} + \frac{\mathbf{v}^+ + \mathbf{v}^-}{2}\cdot\nabla \tag{A.31}$$

is the convective derivative using the average of the local fluid velocities above and below the sheet as the convective velocity. Thus, the doublet wake panels do not change their strength with time and their corners convect with the local fluid velocity.

The influence of a single wake panel on the perturbation velocity can be represented by the influences of four straight line vortex segments at the panel edges. The velocity induced by a straight vortex segment is calculable using the Biot-Savart law[16]

$$\mathbf{v}_{\text{seg}} = -\frac{,}{4\pi}\frac{\mathbf{r}_1\times\mathbf{r}_2}{|\mathbf{r}_1\times\mathbf{r}_2|^2}\left[\frac{\mathbf{r}_2\cdot\mathbf{r}_1}{r_1} - r_1 + \frac{\mathbf{r}_2\cdot\mathbf{r}_1}{r_2} - r_2\right], \tag{A.32}$$

where $\mathbf{r}_1$ and $\mathbf{r}_2$ are the vectors from the end positions of the vortex segment to the observer point such that $\mathbf{r}_1 - \mathbf{r}_2$ lies parallel to the vorticity vector, $\mathbf{\Gamma}$, as shown in Figure (A.2). Care must be taken in the numerical evolution of free, discrete vortices because the veloc-

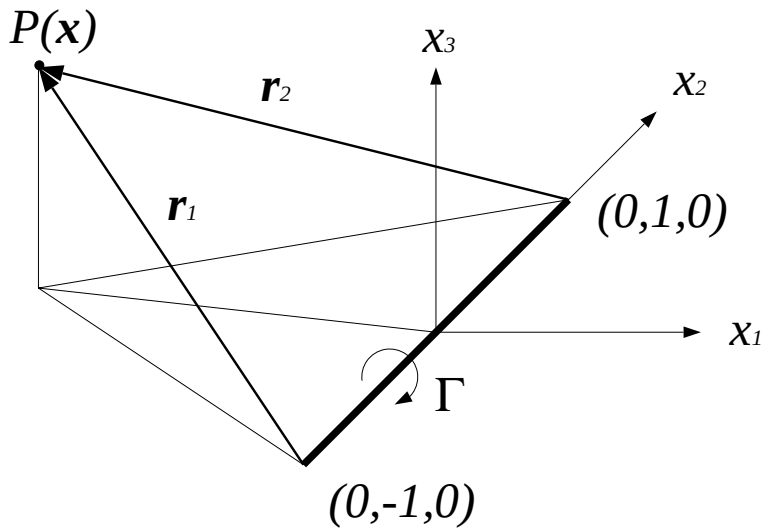

Figure A.2: Schematic of vortex segment.

ities become singular at the vortex cores and wake shapes become unphysical if vortices come within close proximity to one another. This difficulty may be avoided by using *regularization* methods, where a vortex core model is specified to result in a smooth influence

function. A popular regularization of Eq. (A.32) is Krasny's vortex blob method,[8,17] where a regularization parameter, ϵ, is introduced to remove the singularity at the core via

$$\mathbf{v}\mathrm{seg}_{\epsilon} = -\frac{,}{4\pi}\frac{\mathbf{r}_1 \times \mathbf{r}_2}{|\mathbf{r}_1 \times \mathbf{r}_2|^2 + \epsilon^2}\left[\frac{\mathbf{r}_2 \cdot \mathbf{r}_1}{r_1} - r_1 + \frac{\mathbf{r}_2 \cdot \mathbf{r}_1}{r_2} - r_2\right]. \tag{A.33}$$

The effect of this regularization is shown in Figure A.3 for the case of a vortex segment lying between the points $(0,-1,0)$ and $(0,1,0)$. The v_3 component of the induced velocity is shown at varying points along the x_1 axis. Increasing the regularization parameter is seen to smooth the influence around the core and limit the peak influence. For the preliminary results presented in this prospectus, $\epsilon = 0.1$ was chosen in accordance with typical values used in [Ref. 8].

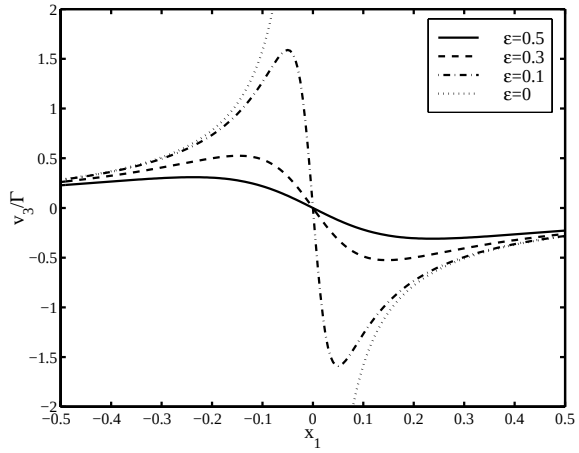

Figure A.3: Influence of a vortex segment using different levels of regularization.

A.3 Supporting Derivation

A.3.1 Potential Aerodynamics

The derivations in this section are well known and is included here only for reference and completeness.

Fundamental Equations

The equations of mass and momentum conservation for an inviscid fluid may be written as

$$\frac{D\rho}{Dt} + \rho\nabla\cdot\mathbf{v} = 0, \tag{A.34}$$

$$\rho\frac{D\mathbf{v}}{Dt} = -\nabla p. \tag{A.35}$$

Assuming adiabatic heat transfer, entropy will be convected purely with the mean flow, *i.e.*,

$$\frac{Ds}{Dt} = 0. \tag{A.36}$$

Thus the First Law of Thermodynamics reduces to

$$dh = \frac{dp}{\rho}. \tag{A.37}$$

The momentum equation (A.35) then becomes

$$\frac{D\mathbf{v}}{Dt} = -\nabla h, \tag{A.38}$$

which implies that if the flow is initially irrotational and there are no sources of vorticity in the flow, then the flow remains irrotational for all subsequent time. Under these circumstances, there exists a velocity potential, ϕ, such that $\mathbf{v} = \nabla\phi$. Equation (A.36) also implies

$$dp = c^2 d\rho, \qquad c^2 = \left.\frac{\partial p}{\partial\rho}\right|_s. \tag{A.39}$$

Writing Eq. (A.38) in terms of the velocity potential and using standard tensor notation gives

$$\frac{\partial}{\partial t}\frac{\partial\phi}{\partial x_j} + \frac{\partial\phi}{\partial x_i}\frac{\partial}{\partial x_i}\frac{\partial\phi}{\partial x_j} = -\frac{1}{\rho}\frac{\partial p}{\partial x_j}, \tag{A.40}$$

$$\frac{\partial}{\partial t}\frac{\partial\phi}{\partial x_j} + \frac{\partial\left(\frac{v^2}{2}\right)}{\partial x_j} = -\frac{\partial h}{\partial x_j}. \tag{A.41}$$

Integrating the above relation in space and assuming that ϕ and its derivatives are zero at infinity gives Bernoulli's Theorem

$$\frac{\partial\phi}{\partial t} + \frac{v^2}{2} = h_\infty - h. \tag{A.42}$$

Similarly, Eq. (A.34) becomes

$$\frac{1}{\rho}\frac{D\rho}{Dt} + \nabla^2\phi = \left.\frac{\partial\rho}{\partial p}\right|_s \frac{Dh}{Dt} + \nabla^2\phi = 0. \tag{A.43}$$

Combining with Eq. (A.42)

$$\nabla^2\phi - \frac{1}{c^2}\frac{D}{Dt}\left[\frac{\partial\phi}{\partial t} + \frac{v^2}{2}\right]. \tag{A.44}$$

In order to obtain a wave equation, we need to relate the speed of sound to the velocity potential. For an ideal gas, the adiabatic relation can be expressed by $p\rho^{-\gamma} = \text{constant}$, where $\gamma = c_p/c_v$ is the ratio of specific heats (assumed constant). This gives

$$c^2 = \frac{\gamma p}{\rho}, \tag{A.45}$$

$$dh = \frac{dp}{\rho} = \gamma\rho^{\gamma-1}\frac{d\rho}{\rho}, \tag{A.46}$$

$$h - h_\infty = \frac{\rho_\infty^\gamma}{p_\infty}\frac{c^2 - c_\infty^2}{\gamma - 1}. \tag{A.47}$$

Thus, Bernoulli's Equation reduces to

$$\frac{\partial\phi}{\partial t} + \frac{v^2}{2} = \frac{\rho_\infty^\gamma}{p_\infty}\frac{c_\infty^2 - c^2}{\gamma - 1}, \tag{A.48}$$

or equivalently,

$$c^2 = c_\infty^2 - \frac{p_\infty}{\rho_\infty^\gamma}(\gamma - 1)\left[\frac{\partial\phi}{\partial t} + \frac{v^2}{2}\right]. \tag{A.49}$$

Combining Equations (A.44) and (A.49) gives

$$\left[c_\infty^2 - \frac{p_\infty}{\rho_\infty^\gamma}(\gamma - 1)\left(\frac{\partial\phi}{\partial t} + \frac{v^2}{2}\right)\right]\nabla^2\phi - \frac{D}{Dt}\left(\frac{\partial\phi}{\partial t} + \frac{v^2}{2}\right) = 0, \tag{A.50}$$

$$c_\infty^2\nabla^2\phi - \frac{\partial^2\phi}{\partial t^2} = (c_\infty^2 - c^2)\nabla^2\phi + \mathbf{v}\cdot\nabla\frac{\partial\phi}{\partial t} + \frac{D\left(\frac{v^2}{2}\right)}{Dt}. \tag{A.51}$$

Thus, we finally obtain a linear wave equation (in the air frame of reference) with nonlinear forcing terms

$$\nabla^2\phi - \frac{1}{c_\infty^2}\frac{\partial^2\phi}{\partial t^2} = \sigma = \frac{1}{c_\infty^2}\left[(c_\infty^2 - c^2)\nabla^2\phi + 2\mathbf{v}\cdot\frac{\partial\mathbf{v}}{\partial t} + \frac{\mathbf{v}}{2}\cdot\nabla v^2\right]. \tag{A.52}$$

Coefficient of Pressure

Recall Equation (A.42)

$$h_\infty - h = \frac{\partial\phi}{\partial t} + \frac{v^2}{2}, \tag{A.53}$$

$$\frac{h - h_\infty}{\frac{1}{2}U_\infty^2} = -\frac{2}{U_\infty^2}\frac{\partial\phi}{\partial t} - \left(\frac{v}{U_\infty}\right)^2. \tag{A.54}$$

For an incompressible fluid, this becomes

$$C_p = \frac{p - p_\infty}{\frac{1}{2}\rho U^2} = -\frac{2}{U^2}\frac{\partial \phi}{\partial t} - \left(\frac{v}{U}\right)^2, \tag{A.55}$$

where U is the velocity of the wing in the air frame of reference.

For a compressible, isentropic fluid, $dh = dp/\rho$ and $p/\rho^\gamma = K = \text{constant}$. Thus,

$$h - h_\infty = \int_{p_\infty}^{p} \frac{dp}{\rho(p)} = \int_{\rho_\infty}^{\rho} K\gamma\rho^{\gamma-2}d\rho = K\frac{\gamma}{\gamma-1}\left(\rho^{\gamma-1} - \rho_\infty^{\gamma-1}\right). \tag{A.56}$$

Assuming that $h = 0$ when $\rho = 0$, then

$$h_\infty = \frac{\gamma}{\gamma-1}\frac{p_\infty}{\rho_\infty} \tag{A.57}$$

and

$$\frac{h - h_\infty}{h_\infty} = \left(\frac{\rho}{\rho_\infty}\right)^{\gamma-1} - 1 = \left(\frac{p}{p_\infty}\right)^{1-\frac{1}{\gamma}} - 1. \tag{A.58}$$

Thus,

$$\frac{p}{p_\infty} = \left[1 - \frac{1}{h_\infty}\left(\dot{\phi} + \frac{v^2}{2}\right)\right]^{\frac{\gamma}{\gamma-1}}. \tag{A.59}$$

Therefore,

$$C_p = \frac{p - p_\infty}{\frac{1}{2}\rho_\infty U^2} = \frac{p_\infty}{\frac{1}{2}\rho_\infty U^2}\left[\left(1 - \frac{\dot{\phi} + \frac{v^2}{2}}{h_\infty}\right)^{\frac{\gamma}{\gamma-1}} - 1\right]. \tag{A.60}$$

Vorticity Transport Theorem

Begin with Euler's equations for an inviscid, isentropic flow

$$\frac{D\mathbf{v}}{Dt} = -\nabla h. \tag{A.61}$$

Taking the curl of both sides

$$\frac{\partial}{\partial t}(\nabla \times \mathbf{v}) + \nabla \times [\mathbf{v} \cdot \nabla \mathbf{v}] = 0. \tag{A.62}$$

Denote the vorticity by $\xi = \nabla \times \mathbf{v}$. Using the identity $\mathbf{v} \cdot \nabla \mathbf{v} = \nabla(v^2/2) - \mathbf{v} \times \xi$, we obtain

$$\frac{\partial \xi}{\partial t} - \nabla \times (\mathbf{v} \times \xi) = 0, \tag{A.63}$$

$$\frac{\partial \xi}{\partial t} - [\xi \cdot \nabla \mathbf{v} - \mathbf{v} \cdot \nabla \xi - \xi \nabla \cdot \mathbf{v} + \mathbf{v} \nabla \cdot \xi] = 0. \tag{A.64}$$

The term $\nabla \cdot \xi = \nabla \cdot (\nabla \times \mathbf{v})$ is zero. This leaves

$$\frac{\partial \xi_i}{\partial t} + \frac{\partial (v_j \xi_i)}{\partial x_j} = \xi_j \frac{\partial v_i}{\partial x_j}, \tag{A.65}$$

$$\frac{D\xi_i}{Dt} + (\nabla \cdot \mathbf{v})\xi_i = (\xi \cdot \nabla) v_i. \tag{A.66}$$

Kelvin's Theorem

Choose a closed contour, C, which encloses the same fluid elements for all time. The rate of change of circulation of the fluid within this contour is

$$\begin{aligned}\frac{D,}{Dt} &= \frac{D}{Dt}\oint_C \mathbf{v}\cdot d\mathbf{l} = \oint_C \frac{D}{Dt}(\mathbf{v}\cdot d\mathbf{l}) = \oint_C \frac{D\mathbf{v}}{Dt}\cdot d\mathbf{l} + \oint_C \mathbf{v}\cdot d\mathbf{v}, \\ &= -\oint_C \nabla h\cdot d\mathbf{l} + \oint_C d\frac{\mathbf{v^2}}{\mathbf{2}} = 0. \end{aligned} \tag{A.67}$$

Note also that

$$, = \oint_C \mathbf{v}\cdot d\mathbf{l} = \iint_A (\nabla\times\mathbf{v})\cdot\hat{n}dS = \iint_A \xi\cdot\hat{n}dS. \tag{A.68}$$

In the limit as $A\to 0$, $d,\ = \xi\cdot\hat{n}dA =$ constant, if ξ is continuous in dA. Therefore, for arbitrary dA and $\hat{n}$, $\xi\equiv 0$ if the fluid in dA was initially irrotational. Thus, in these regions of the fluid (excluding the wake where γ is not initially zero), there exists a velocity potential, ϕ, such that $\mathbf{v}=\nabla\phi$.

A.3.2 Kirchhoff Methods

Kirchhoff methods are used to predict quantities satisfying a scalar wave equation in the field surrounding a surface on which the variable and its derivatives are known. For a wave phenomenon described by the partial differential equation

$$\mathcal{L}[\phi] = \sigma, \tag{A.69}$$

in the physical field (e.g., exterior to a wing), where $\mathcal{L}$ is a linear, self-adjoint differential operator. The Green's function is chosen to satisfy the equation

$$\mathcal{L}_{(\mathbf{y},\tau)}[G(\mathbf{x},t|\mathbf{y},\tau)] = \delta(\mathbf{x}-\mathbf{y})\delta(t-\tau), \tag{A.70}$$

and the boundary conditions at infinity.

Let the surface, S, be given by the equation

$$f(\mathbf{x},t) = 0, \tag{A.71}$$

where f is a sufficiently differentiable function (depending on the order of $\mathcal{L}$) normalized in such a way so that the equation

$$\left.\frac{\nabla f}{|\nabla f|}\right|_{\text{on S}} = \hat{\mathbf{n}} \tag{A.72}$$

defines the outward unit normal to S. To account for the surface effects of ϕ, consider the generalized function, $H(f)\phi$, defined in all space. Treating the derivatives in $\mathcal{L}$ as generalized derivatives, applying to $H(f)\phi$, and using

$$\frac{\partial}{\partial x_i}H(f(\mathbf{x})) = \frac{\partial f}{\partial x_i}\delta(f) = \hat{n}_i\delta(f), \tag{A.73}$$

$$\frac{\partial}{\partial t}H(f(\mathbf{x})) = \frac{\partial x_i}{\partial t}\frac{\partial f}{\partial x_i}\delta(f) = -v_n\delta(f), \tag{A.74}$$

gives

$$\mathcal{L}[H(f)\phi] = H\mathcal{L}\phi + \mathcal{F} = H\sigma + \mathcal{F}, \tag{A.75}$$

where $\mathcal{F}$ describes the surface sources. If the boundary conditions at infinity are homogeneous, then multiplying Eq. (A.70) by ϕ, Eq. (A.75) by G, and integrating over all $(\mathbf{y},\tau)$ gives the integral equation

$$\begin{aligned} H(f)\phi(\mathbf{x},t) &= \int G(\mathbf{x},t|\mathbf{y},\tau)\left[H(f(\mathbf{y}))\phi(\mathbf{y},\tau) + \mathcal{F}(\mathbf{y},\tau)\right]d\mathbf{y}d\tau \\ &= \int_{-\infty}^{t}\int_{V} G\sigma dV d\tau + \int G\mathcal{F}d\mathbf{y}d\tau. \end{aligned} \tag{A.76}$$

When there are no sources in the field, V, the first integral above vanishes. The second integral will be over the surface, S, because $\mathcal{F}$ will contain $\delta(f)$ and its derivatives. The result will be an integral equation relating ϕ in the field, V, to ϕ and its derivatives on the surface, S. If ϕ is known on the surface, then the field is determined directly by evaluating the integral. Conversely, by choosing the observer locations, $\mathbf{x}$, to lie on the surface, a consistency relation is obtained from which ϕ may be determined implicitly on the surface by solving the integral equation via panel, or boundary element, methods. In the following sections, Kirchhoff equations will be derived for various differential operators of interest.

Classical Wave Equation

Applying Equation (A.76) to the classical wave equation for a motionless surface, S, gives the classical Kirchhoff equation (c. 1882). The operator $\mathcal{L}$ is given here by

$$\mathcal{L} = \frac{1}{c^2}\frac{\partial^2}{\partial t^2} - \nabla^2. \tag{A.77}$$

Note that

$$\begin{aligned} \frac{\partial}{\partial t^2}(H(f)\phi) &= H\ddot{\phi} - v_n\dot{\phi}\delta - \frac{\partial}{\partial t}(v_n\phi\delta), \\ \frac{\partial}{\partial x_i^2}(H(f)\phi) &= H\phi_{x_ix_i} + \frac{\partial\phi}{\partial n}\delta + \frac{\partial}{\partial x_i}(n_i\phi\delta). \end{aligned} \tag{A.78}$$

The surface sources are thus

$$\mathcal{F} = -\left(\frac{M_n}{c}\dot{\phi} + \frac{\partial\phi}{\partial n}\right)\delta(f) - \frac{\partial}{\partial\tau}\left(\frac{M_n}{c}\phi\delta(f)\right) - \frac{\partial}{\partial y_i}\left(n_i\phi\delta(f)\right). \tag{A.79}$$

For a motionless surface, $v_n = 0$, and

$$\mathcal{F} = -\frac{\partial\phi}{\partial n}\delta(f) - \frac{\partial}{\partial y_i}\left(n_i\phi\delta(f)\right). \tag{A.80}$$

The Green's function satisfying the radiation condition is

$$\begin{aligned} G(\mathbf{x},t|\mathbf{y},\tau) &= \frac{\delta(g)}{4\pi r}, \\ g &= \tau - t + \frac{r}{c}, \\ r &= \sqrt{(x_1-y_1)^2 + (x_2-y_2)^2 + (x_3-y_3)^2}. \end{aligned} \tag{A.81}$$

Note that

$$\frac{\partial G}{\partial x_i} = -\frac{\partial G}{\partial y_i}, \qquad \frac{\partial G}{\partial t} = -\frac{\partial G}{\partial\tau}. \tag{A.82}$$

Applying Equation (A.76) gives

$$H(f)\phi(\mathbf{x},t) = \int\int_V G\sigma dV d\tau - \int\int_S G\frac{\partial\phi}{\partial n}dSd\tau - \int G\frac{\partial}{\partial y_i}(n_i\phi\delta(f))d\mathbf{y}d\tau. \tag{A.83}$$

Integrating the last integral by parts and applying eqs. (A.82) gives

$$4\pi H(f)\phi(\mathbf{x},t) = \int_V \left[\frac{\sigma}{r}\right]_{\tau^\star} dV - \int_S \left[\frac{1}{r}\frac{\partial\phi}{\partial n}\right]_{\tau^\star} dS - 4\pi\frac{\partial}{\partial x_i}\int G(n_i\phi\delta)d\mathbf{y}d\tau, \tag{A.84}$$

where $\tau^\star = t - r/c$ is the solution to the equation $g(\tau) = 0$ and is referred to as the retarded time. The integrals above represent volume sources, surface sources, and surface

dipoles respectively. The dipole integral may be simplified by converting spatial to temporal derivatives. Note that

$$\frac{\partial g}{\partial \tau} = 1, \qquad \frac{\partial g}{\partial x_i} = \frac{\hat{r}_i}{c}, \tag{A.85}$$

where $\hat{r}_i = (x_i - y_i)/r$. Thus,

$$\frac{\partial G}{\partial x_i} = -\frac{\hat{r}_i}{r^2}\delta(g) + \frac{1}{r}\frac{\hat{r}_i}{c}\frac{\partial}{\partial \tau}\delta(g). \tag{A.86}$$

Substituting the above into the integral equation and integrating by parts in time gives

$$4\pi H(f)\phi(\mathbf{x},t) \;=\; \int\limits_V \left[\frac{\sigma}{r}\right]_{\tau^\star} dV - \int\limits_S \left[\frac{1}{r}\frac{\partial \phi}{\partial n} + \frac{\cos\theta}{r^2}\phi + \frac{\cos\theta}{rc}\dot{\phi}\right]_{\tau^\star} dS, \tag{A.87}$$

where $\cos\theta = \hat{\mathbf{r}} \cdot n$.

Convective Wave Equation

The convective wave operator may be written

$$\mathcal{L} = \frac{1}{c^2}\frac{D^2}{Dt^2} - \nabla^2 = \left[\frac{1}{c}\left(\frac{\partial}{\partial t} + \mathbf{u}\cdot\nabla\right)\right]^2 - \nabla^2, \tag{A.88}$$

where $\mathbf{u}$ is the convective fluid velocity. Consider the surface, S, to be translating at constant velocity, $-U_\infty \hat{i}$. In the moving frame of reference, S appears motionless and $\mathbf{u} = U_\infty \hat{i}$. Scaling space with L, a characteristic length of S, and time with L/U_∞, the operator becomes

$$\mathcal{L} = M^2\left[\frac{\partial}{\partial t} + \frac{\partial}{\partial x_1}\right]^2 - \nabla^2 = M^2\left[\frac{\partial^2}{\partial t^2} + 2\frac{\partial^2}{\partial x_1 \partial t} + \frac{\partial^2}{\partial x_1^2}\right] - \nabla^2. \tag{A.89}$$

For constant M, the convective wave equation may be written in the form of the classical wave equation by stretching and shifting space-time appropriately; *i.e.*, the differential operator is diagonalized by using the Prandtl-Glauert transformation (c. 1922-27),

$$\{\tilde{x}_1, \tilde{x}_2, \tilde{x}_3\} = \{x_1/\beta, x_2, x_3\}, \tag{A.90}$$

and a temporal transformation of the form

$$\tilde{t} = t + \theta(x_1), \tag{A.91}$$

to eliminate the cross derivatives. Denote $\tilde{\phi}(\tilde{\mathbf{x}}, \tilde{t}) = \phi(\mathbf{x}, t)$, and note that

$$\begin{aligned} \frac{\partial \phi}{\partial t} &= \frac{\partial \tilde{\phi}}{\partial \tilde{t}}, \\ \frac{\partial \phi}{\partial x_1} &= \frac{1}{\beta}\frac{\partial \tilde{\phi}}{\partial \tilde{x}_1} + \theta'\frac{\partial \tilde{\phi}}{\partial \tilde{t}}. \end{aligned} \tag{A.92}$$

Substituting the above into the wave equation gives

$$\left\{ M^2 \left[\partial_{\tilde{t}} + \left(\frac{1}{\beta} \partial_{\tilde{x}_1} + \theta' \partial_{\tilde{t}} \right) \right]^2 - \left(\frac{1}{\beta} \partial_{\tilde{x}_1} + \theta' \partial_{\tilde{t}} \right)^2 - \partial_{\tilde{x}_2 \tilde{x}_2} - \partial_{\tilde{x}_3 \tilde{x}_3} \right\} \tilde{\phi} \;=\; 0. \quad \text{(A.93)}$$

Collecting like terms gives

$$\left\{ \left[M^2 (1+\theta')^2 - (\theta')^2 \right] \partial_{\tilde{t}\tilde{t}} - \tilde{\nabla}^2 + \frac{2}{\beta} \left[M^2 (1+\theta') - \theta' \right] \partial_{\tilde{t}\tilde{x}_1} \right\} \tilde{\phi} \;=\; 0 \quad \text{(A.94)}$$

The cross derivative disappears if we set

$$\theta(x_1) = \frac{M^2 x_1}{\beta^2}. \quad \text{(A.95)}$$

Denoting $\tilde{c} = \beta/M$ and using $\tilde{t} = t + x_1/\tilde{c}^2$, the convective wave equation is written in classical form

$$\left[\frac{1}{\tilde{c}^2} \frac{\partial^2}{\partial \tilde{t}^2} - \tilde{\nabla}^2 \right] \tilde{\phi}(\tilde{\mathbf{x}}, \tilde{t}) = \tilde{\sigma}. \quad \text{(A.96)}$$

The free-space Green's function is now easily recognized in the physical dimensionless coordinates as

$$G(\mathbf{x}, t | \mathbf{y}, \tau) = \frac{1}{4\pi r_\beta} \delta \left[\tau - t + \frac{M}{\beta} \left(r_\beta - \frac{M x_1}{\beta} \right) \right], \quad \text{(A.97)}$$

where $r_\beta = \sqrt{(x_1 - y_1)^2/\beta^2 + [(x_3 - y_3)^2 + (x_3 - y_3)^2]}$. In the frequency domain using $\phi = \hat{\phi} \exp(-i\omega t)$,

$$G(\mathbf{x}|\mathbf{y}) = \frac{e^{i \frac{\omega M}{\beta} (r_\beta - M x_1/\beta)}}{4\pi r_\beta}, \quad \text{(A.98)}$$

where ω is the dimensionless frequency scaled by U_∞/L.

Applying the classical Kirchhoff equation in Reissner space and transforming back to physical coordinates gives

$$4\pi H(f) \phi(\mathbf{x}, t) \;=\; \int_V \left[\frac{\tilde{\sigma}}{r_\beta} \right]_{\tau^\star} dV - \int_S \left[\frac{1}{r_\beta} \frac{\partial \tilde{\phi}}{\partial \tilde{n}} + \frac{\cos\tilde{\theta}}{r_\beta^2} \phi + \frac{M \cos\tilde{\theta}}{\beta r_\beta} \dot{\phi} \right]_{\tau^\star} \frac{dS}{\beta}, \quad \text{(A.99)}$$

where $\cos\tilde{\theta} = \hat{\tilde{\mathbf{r}}} \cdot \tilde{\mathbf{n}}$, and

$$\tau^\star \;=\; t - \frac{M}{\beta} \left(r_\beta - \frac{M x_1}{\beta} \right). \quad \text{(A.100)}$$

Note that $\tilde{f}(\tilde{\mathbf{x}}) = f(\mathbf{x})$, and

$$d\tilde{S} = \delta \left(\tilde{f}(\tilde{\mathbf{x}}) \right) d\tilde{x}_1 d\tilde{x}_2 d\tilde{x}_3 = \delta \left(f(\mathbf{x}) \right) \frac{dx_1 dx_2 dx_3}{\beta} = \frac{dS}{\beta}. \quad \text{(A.101)}$$

Caution is needed in interpreting the normal vector because of the Prandtl-Glauert and Reissner transformations. Note that

$$\mathbf{n} = \frac{\nabla f}{|\nabla f|}, \tag{A.102}$$

$$\tilde{\mathbf{n}} = \frac{\tilde{\nabla} f}{|\tilde{\nabla} f|} = \{\beta n_1, n_2, n_3\} \frac{|\nabla f|}{|\tilde{\nabla} f|}, \tag{A.103}$$

and that

$$\frac{|\tilde{\nabla} f|}{|\nabla f|} = \sqrt{1 - M^2 n_1^2} \tag{A.104}$$

$$\tilde{\nabla} \tilde{\phi} = \{\beta(\partial_{x_1} - \theta' \partial_t), \partial_{x_2}, \partial_{x_3}\} \phi \tag{A.105}$$

Therefore,

$$\frac{\partial \tilde{\phi}}{\partial \tilde{n}} = \frac{\frac{\partial \phi}{\partial n} - M^2 n_1 (\partial_t + \partial_{x_1}) \phi}{\sqrt{1 - M^2 n_1^2}}, \tag{A.106}$$

$$\cos \tilde{\theta} = \hat{\tilde{\mathbf{r}}} \cdot \tilde{\mathbf{n}} = \frac{\mathbf{r} \cdot \mathbf{n}}{\sqrt{1 - M^2 n_1^2}} = \frac{\cos \theta}{\sqrt{1 - M^2 n_1^2}}. \tag{A.107}$$

The above spatial derivative may be written in terms of a surface gradient by expressing the unit vectors in normal and tangential components; *i.e.*,

$$\hat{\imath} = (\hat{\imath} \cdot \mathbf{n}) \mathbf{n} + (\hat{\imath} \cdot t_1) \mathbf{t}_1 = n_1 \mathbf{n} + t_{11} \mathbf{t}_1, \tag{A.108}$$

where,

$$\mathbf{t}_1 = \frac{\hat{\imath} - n_1 \mathbf{n}}{t_{11}} = \frac{\hat{\imath} - n_1 \mathbf{n}}{\sqrt{1 - n_1^2}} \tag{A.109}$$

Thus, the spatial derivative may be written as

$$\frac{\partial \phi}{\partial x_1} = \hat{\imath} \cdot \nabla \phi = n_1 \frac{\partial \phi}{\partial n} + \sqrt{1 - n_1^2} \frac{\partial \phi}{\partial t_1} \tag{A.110}$$

Therefore,

$$\frac{\partial \tilde{\phi}}{\partial \tilde{n}} = \frac{\frac{\partial \phi}{\partial n}(1 - M^2 n_1^2) - M^2 n_1 \dot{\phi} - M^2 n_1 \sqrt{1 - n_1^2} \frac{\partial \phi}{\partial t_1}}{\sqrt{1 - M^2 n_1^2}}. \tag{A.111}$$

Finally, the Kirchhoff equation for a motionless surface placed in a uniform, subsonic flow (in the x_1 direction) is

$$4\pi H(f) \phi(\mathbf{x}, t) = \int_V \left[\frac{\tilde{\sigma}}{r_\beta}\right]_{\tau^\star} dV - \int_S \frac{1}{r_\beta \sqrt{1 - M^2 n_1^2}} \times \tag{A.112}$$

$$\left[\left(1 - M^2 n_1^2\right) \frac{\partial \phi}{\partial n} + \frac{\cos \theta}{r_\beta} \phi + \left(\frac{\cos \theta}{\beta} - M n_1\right) M \dot{\phi} - M^2 n_1 \sqrt{1 - n_1^2} \frac{\partial \phi}{\partial t_1}\right]_{\tau^\star} \frac{dS}{\beta}.$$

A.3.3 Boundary Element Method

In this appendix, a method for solving integral equations known as the Boundary Element Method is presented. This will be done by first demonstrating the application of the method on the standard Kirchhoff solution to Laplace's equation given by Eq. (A.87) without the volume integral; *i.e.*, neglect the effects of the nonlinear sources and compressibility.

Divide the surface of integration into N panels such that $S = \{S_j\}_{j=1}^{N}$. The integral equation then becomes

$$4\pi H(f)\phi(\mathbf{x},t) = \sum_{j=1}^{N} \int_{S_j} \left[\frac{\partial}{\partial n}\left(\frac{1}{r}\right)\phi - \frac{1}{r}\frac{\partial \phi}{\partial n} \right] dS, \tag{A.113}$$

As in the Finite Element method, introduce a set of *shape functions*, $\psi_k(\mathbf{x})$, which form a basis which can be used to describe the unknown functions through a relation of the type

$$\phi(\mathbf{x},t) = \sum_{p=1}^{P} \psi_p(\mathbf{x})\phi_p(t). \tag{A.114}$$

The shape functions are chosen such that $\psi_k(\mathbf{x}_i) = \delta_{ik}$ for P specially chosen points on the panel known as the *collocation points*. Let the set of M distinct collocation points for the entire integration surface be denoted by $\{\mathbf{x}_i\}_i^M$. Evaluating the integral equation at these collocation points (where $H(f) = 0.5$ because $f = 0$ on the surface S) gives

$$2\pi\phi(\mathbf{x}_i,t) = \sum_{j,k=1}^{N,P} \left[G_{D_{ijk}}\phi_{jk}(t) - G_{S_{ijk}}\left(\frac{\partial\phi}{\partial n}\right)_{jk} \right] dS, \tag{A.115}$$

where,

$$G_{D_{ijk}} = \int_{S_j} \frac{\partial}{\partial n}\left(\frac{1}{\|\mathbf{x}_i - \mathbf{y}\|}\right)\psi_k(\mathbf{y})dS, \tag{A.116}$$

$$G_{S_{ijk}} = \int_{S_j} \frac{1}{\|\mathbf{x}_i - \mathbf{y}\|}\psi_k(\mathbf{y})dS, \tag{A.117}$$

are the dipole (doublet) and monopole (source) influence tensors respectively. Equation (A.115) can be reduced by applying $NP - M$ constraint equations for coincident ϕ_{jk} where adjacent panels share collocation points on their edges. This leaves M unknown values of ϕ which may be calculated by matrix inversion when the normal derivatives are known via the boundary conditions.

Zeroth Order BEM

The simplest form of Eq. (A.115) is obtained when the unknowns are assumed constant over each panel. This defines a *zeroth order* boundary element method where $P = 1$, and $\psi_1(\mathbf{x}) = 1$ on the panel (0 elsewhere). The collocation points are chosen to be located at the

centers of each panel. The matrix equation becomes

$$2\pi\phi(\mathbf{x}_i,t) = \sum_j^N \left[G_{D_{ij}}\phi_j(t) - G_{S_{ij}}\left(\frac{\partial\phi}{\partial n}\right)_j \right] dS, \tag{A.118}$$

$$G_{D_{ij}} = \int_{S_j} \frac{\partial}{\partial n}\left(\frac{1}{\|\mathbf{x}_i-\mathbf{y}\|}\right) dS, \tag{A.119}$$

$$G_{S_{ij}} = \int_{S_j} \frac{1}{\|\mathbf{x}_i-\mathbf{y}\|} dS. \tag{A.120}$$

Analytical Form of Influence Matrices

The dipole and source influence functions are known analytically for hyperboloidal and flat panels, respectively;[14,16,18] however, the analytical source influence function may be used as an approximation for 'nearly' flat hyperboloidal panels.

Consider the influence of a single hyperboloidal surface element. Any point on the element may be described by

$$\mathbf{r} = \mathbf{c}_0 + \xi\mathbf{c}_1 + \eta\mathbf{c}_2 + \xi\eta\mathbf{c}_3, \tag{A.121}$$

where (ξ,η) are local panel coordinates and the panel domain may be taken as $-1 \le \xi \le 1$ and $-1 \le \eta \le 1$. The coefficient vectors for the panel may be determined by

$$\begin{Bmatrix} \mathbf{c}_0 \\ \mathbf{c}_1 \\ \mathbf{c}_2 \\ \mathbf{c}_3 \end{Bmatrix} = \frac{1}{4}\begin{bmatrix} 1 & 1 & 1 & 1 \\ 1 & 1 & -1 & -1 \\ 1 & -1 & 1 & -1 \\ 1 & -1 & -1 & 1 \end{bmatrix} \begin{Bmatrix} \mathbf{p}_{++} \\ \mathbf{p}_{+-} \\ \mathbf{p}_{-+} \\ \mathbf{p}_{--} \end{Bmatrix}, \tag{A.122}$$

where $\{\mathbf{p}_{--},\mathbf{p}_{+-},\mathbf{p}_{++},\mathbf{p}_{-+}\}$ are the positions of the panel corners arranged counterclockwise as viewed from above the panel.

The influence functions for the panel may be expressed in the form[14]

$$G_{D_{ij}} = I_D(1,1) - I_D(-1,1) - I_D(1,-1) + I_D(-1,-1), \tag{A.123}$$

$$G_{S_{ij}} = I_S(1,1) - I_S(-1,1) - I_S(1,-1) + I_S(-1,-1), \tag{A.124}$$

where

$$I_D(\xi,\eta) = \tan^{-1}\left[\frac{\mathbf{R}\times\mathbf{a}_1\cdot\mathbf{R}\times\mathbf{a}_2}{|\mathbf{R}|\mathbf{R}\cdot\mathbf{a}_1\times\mathbf{a}_2}\right], \tag{A.125}$$

$$\begin{aligned} I_S(\xi,\eta) = & -\mathbf{R}\times\frac{\mathbf{a}_1}{|\mathbf{a}_1|}\cdot\mathbf{n}_c \sinh^{-1}\left(\frac{\mathbf{R}\cdot\mathbf{a}_1}{|\mathbf{R}\times\mathbf{a}_1|}\right) \\ & +\mathbf{R}\times\frac{\mathbf{a}_2}{|\mathbf{a}_2|}\cdot\mathbf{n}_c \sinh^{-1}\left(\frac{\mathbf{R}\cdot\mathbf{a}_2}{|\mathbf{R}\times\mathbf{a}_2|}\right) + \mathbf{R}_c\cdot\mathbf{n}_c I_D(\xi,\eta), \end{aligned} \tag{A.126}$$

and

$$\mathbf{R}(\xi,\eta) = \mathbf{r} - \mathbf{x}_i, \tag{A.127}$$

$$\mathbf{a}_1(\xi,\eta) = \frac{\partial \mathbf{R}}{\partial \xi} = \mathbf{c}_1 - \eta \mathbf{c}_3, \tag{A.128}$$

$$\mathbf{a}_2(\xi,\eta) = \frac{\partial \mathbf{R}}{\partial \eta} = \mathbf{c}_2 - \xi \mathbf{c}_3, \tag{A.129}$$

$$\mathbf{n}(\xi,\eta) = \frac{\mathbf{a}_1 \times \mathbf{a}_2}{|\mathbf{a}_1 \times \mathbf{a}_2|}. \tag{A.130}$$

The subscript c denotes evaluation at the panel center, $\xi = \eta = 0$. Equation (A.126) neglects only the derivatives of $\mathbf{n}$ and, hence, is valid only for approximately flat panels. Equation (A.125) is exact, however care must be taken in choosing the correct branch for the arctangent. For flat panels, the principle branch, $-\pi/2 \leq \tan^{-1} x \leq \pi/2$, may be used. Otherwise, when the influence point, $\mathbf{x}_i$, lies outside of the tetrahedron defined by the panel corners, the following procedure is found to work well:

$$\begin{aligned} s(\xi,\eta) &= \text{sign}(\mathbf{R} \cdot \mathbf{a}_1 \times \mathbf{a}_2) \\ S &= s(1,1) + s(1,-1) + s(-1,1) + s(-1,-1) \end{aligned}$$

$$\begin{aligned} &\text{IF} && S = 1 \quad \text{OR} \quad S = -1 \\ &\text{THEN} && G_{D_{ij}} = G_{D_{ij}} - \text{sign}(S)\frac{\pi}{2} \\ &\text{ELSE IF} && S = 2 \quad \text{OR} \quad S = -2 \\ &\text{THEN} && G_{D_{ij}} = G_{D_{ij}} - \text{sign}(S)\pi \\ &\text{ELSE IF} && S = 3 \quad \text{OR} \quad S = -3 \\ &\text{THEN} && G_{D_{ij}} = G_{D_{ij}} - \text{sign}(S)\frac{\pi}{2} \end{aligned} \tag{A.131}$$

B Cases from [1]

C ASME IMECE conference paper. 3D validations